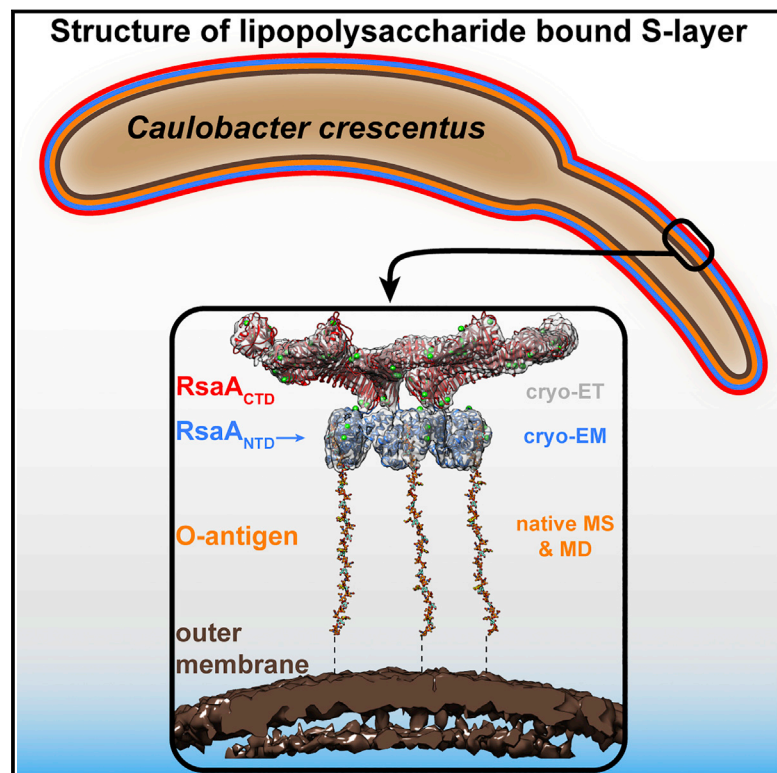# *In Situ* Structure of an Intact Lipopolysaccharide-Bound Bacterial Surface Layer

Graphical Abstract

Authors

Andriko von Kügelgen, Haiping Tang, Gail G. Hardy, ..., Phillip J. Stansfeld, Carol V. Robinson, Tanmay A.M. Bharat

Correspondence

tanmay.bharat@path.ox.ac.uk

In Brief

Cryo-electron tomography allows structure determination of the bacterial S-layer in its cellular context at near-atomic resolution, providing insights into how it's assembled and organized.

Highlights

- 3.7 Å cryo-EM structure of S-layer bound to O-antigen of lipopolysaccharide (LPS)

- MD simulations and native MS show Ca^{2+}-dependent S-layer binding to LPS

- 4.8 Å *in situ* cryo-ET structure of the S-layer on *Caulobacter crescentus* cells

- Integrated structural biology reveals principles of LPS-mediated S-layer assembly

CellPress

In Situ Structure of an Intact Lipopolysaccharide-Bound Bacterial Surface Layer

Andriko von Kügelgen,[1,2] Haiping Tang,[3] Gail G. Hardy,[4] Danguole Kureisaite-Ciziene,[5] Yves V. Brun,[4,6] Phillip J. Stansfeld,[7] Carol V. Robinson,[3] and Tanmay A.M. Bharat[1,2,8,*]

[1]Sir William Dunn School of Pathology, University of Oxford, South Parks Road, Oxford OX1 3RE, United Kingdom
[2]Central Oxford Structural Microscopy and Imaging Centre, South Parks Road, Oxford OX1 3RE, United Kingdom
[3]Physical and Theoretical Chemistry Laboratory, University of Oxford, South Parks Road, Oxford OX1 3TA, United Kingdom
[4]Department of Biology, Indiana University, Bloomington, IN 47405, USA
[5]Structural Studies Division, MRC Laboratory of Molecular Biology, Cambridge CB2 0QH, United Kingdom
[6]Département de microbiologie, infectiologie et immunologie, Université de Montréal, C.P. 6128, Succ. Centre-ville, Montréal, QC H3C 3J7, Canada
[7]Department of Biochemistry, University of Oxford, South Parks Road, Oxford OX1 3QU, United Kingdom
[8]Lead Contact
*Correspondence: tanmay.bharat@path.ox.ac.uk
https://doi.org/10.1016/j.cell.2019.12.006

SUMMARY

Most bacterial and all archaeal cells are encapsulated by a paracrystalline, protective, and cell-shape-determining proteinaceous surface layer (S-layer). On Gram-negative bacteria, S-layers are anchored to cells via lipopolysaccharide. Here, we report an electron cryomicroscopy structure of the *Caulobacter crescentus* S-layer bound to the O-antigen of lipopolysaccharide. Using native mass spectrometry and molecular dynamics simulations, we deduce the length of the O-antigen on cells and show how lipopolysaccharide binding and S-layer assembly is regulated by calcium. Finally, we present a near-atomic resolution *in situ* structure of the complete S-layer using cellular electron cryotomography, showing S-layer arrangement at the tip of the O-antigen. A complete atomic structure of the S-layer shows the power of cellular tomography for *in situ* structural biology and sheds light on a very abundant class of self-assembling molecules with important roles in prokaryotic physiology with marked potential for synthetic biology and surface-display applications.

INTRODUCTION

Most bacterial and all archaeal cells are encapsulated by a paracrystalline, sheet-like, proteinaceous sheath known as a surface layer (or S-layer) (Sára and Sleytr, 2000). S-layers are made up of two-dimensional lattices built by repeated interactions between a special class of proteins called S-layer proteins (Sleytr et al., 2014). Due to high-copy numbers of S-layer proteins in prokaryotic cells, it is estimated that S-layer proteins are the most abundant class of proteins on earth (Pum et al., 2013). S-layers play critical roles in prokaryotic physiology, ranging from cell-shape

determination to protection from predators and phages (Sleytr et al., 2014). Since the first observation of S-layers over half a century ago (Houwink, 1953), structural biology information on S-layers has been scarce because of the inherent difficulty in studying these flexible two-dimensional arrays using the available structural biology techniques. Pioneering electron microscopy investigations have revealed the low-resolution organization of S-layer lattices (Lupas et al., 1994; Smit et al., 1992; Sumper et al., 1990); however, only a few atomic structures of purified S-layer domains have been reported thus far (Arbing et al., 2012; Baranova et al., 2012; Bharat et al., 2017).

Even less is known at the atomic level about how S-layers are anchored and assembled on cells. In archaeal cells, S-layers are often directly bound to the cell membrane (Albers and Meyer, 2011), and Gram-positive bacterial S-layers are buried in the cell wall (Fagan and Fairweather, 2014; Sára and Sleytr, 2000). In Gram-negative bacteria such as *Caulobacter crescentus* or *Campylobacter fetus*, S-layers are retained on cells by lipopolysaccharide (LPS) or endotoxin molecules present in the outer membrane (OM) (Fagan and Fairweather, 2014; Sára and Sleytr, 2000). LPS of Gram-negative bacteria is an abundant glycolipid responsible for bacterial recognition by foreign agents such as the human immune system or bacteriophages. LPS consists of lipid A, core oligosaccharides (OSs), and a repetitive O-antigen polysaccharide (PS) (Cabeen et al., 2010). Recent structural studies on the LPS have focused on O-antigen secretion through the inner membrane (Bi et al., 2018; Caffalette et al., 2019), LPS transport across the periplasm (Li et al., 2019; Owens et al., 2019), and its subsequent secretion through the OM (Dong et al., 2014; Qiao et al., 2014). However, there is limited information on O-antigen structure (Steinbacher et al., 1996); therefore, its native arrangement and conformation on cells remains enigmatic.

To study the structure, anchoring, and assembly of S-layers on LPS molecules in the OM of Gram-negative bacteria, we turned to *C. crescentus*, a well-studied model bacterium with a complex life cycle (Poindexter, 1964). The S-layer of *C. crescentus* is

composed of a single, 1026-amino-acid-residue, multi-domain, S-layer protein called RsaA (Smit et al., 1992). We have recently reported the X-ray structure of the C-terminal domain of RsaA (RsaA$_{CTD}$), consisting of residues 250–1026, which form the highly interconnected outer S-layer lattice (Bharat et al., 2017). However, the structure of the N-terminal domain of RsaA (RsaA$_{NTD}$), consisting of residues 1–249, which is a putative LPS-binding domain directly proximal to the OM (Bharat et al., 2017; Ford et al., 2007), is as yet unreported. Therefore, how RsaA is tethered to cells via LPS molecules and the native structure and conformation of LPS on cells beneath the S-layer are all unknown.

Here in this study, we have solved the missing structure of the RsaA$_{NTD}$ bound to the O-antigen of the LPS using single-particle electron cryomicroscopy (cryo-EM). Using native mass spectrometry (MS), we studied the calcium (Ca^{2+}) dependence and stoichiometry of sugar binding to RsaA, allowing us to estimate the length of the native O-antigen and understand the architecture of the cellular LPS. Next, molecular dynamics (MDs) simulations combined with electron cryotomography (cryo-ET) allowed us to probe the assembly mechanism of the S-layer on cells. Finally, we used advanced subtomogram averaging techniques to resolve a near-atomic resolution structure of the cellular S-layer, providing unprecedented insights into the S-layer and LPS structure at the *C. crescentus* cell surface. In summary, we report an atomic-level structure of the complete cellular S-layer bound to LPS and multiple Ca^{2+} ions as it is found on the surface of bacterial cells, providing detailed information on S-layer organization and assembly on LPS.

RESULTS

Biochemical Reconstitution and Cryo-EM Analysis of RsaA Binding to LPS

To investigate cellular anchoring of RsaA on LPS, we reconstituted RsaA binding to LPS *in vitro* and studied the assembled complex using single-particle cryo-EM. A mutant *C. crescentus* strain that carried a tobacco etch virus (TEV) cleavage site between RsaA$_{NTD}$ and RsaA$_{CTD}$ after position 250 was used to purify RsaA$_{NTD}$ (STAR Methods). Purified RsaA$_{NTD}$ was primarily monomeric in solution and appeared as small particles on cryo-EM grids (Figures S1A and S1D). Next, we purified the *C. crescentus* LPS from a mutant strain that lacked *rsaA* and added it to RsaA$_{NTD}$. Large oligomers of RsaA$_{NTD}$ were formed around aggregates of crude LPS (Figures S1B, S1D, and S1E). To separate RsaA$_{NTD}$ bound to LPS aggregates into homogeneous single particles, we pretreated the purified crude LPS with acetic acid to cleave off lipid A (Jones et al., 2015), yielding partially cleaved PS. On addition of this PS to RsaA$_{NTD}$, an oligomeric complex of approximately 650 kDa was obtained, which appeared as separated single particles on cryo-EM grids (Figures S1C, S1D, and S1F). Different views of the complex were observed, and top views of the complex were reminiscent of the inner domain of the *C. crescentus* S-layer on cells (Figure 1A) (Bharat et al., 2017; Smit et al., 1992).

We resolved a density map of the RsaA$_{NTD}$:PS complex at 3.7 Å resolution using single-particle cryo-EM techniques (Scheres, 2012). All secondary structure elements and amino

acid side chains were unambiguously assigned, and no significant resolution anisotropy was observed within each RsaA$_{NTD}$ monomer in the cryo-EM map (Figure S2). We used the cryo-EM map to build an atomic model of RsaA$_{NTD}$ along with the bound PS (Figures 1B, 1C, and S2; Video S1; Table S1). In the complex, several copies of RsaA$_{NTD}$ are arranged in a spiral, which is held together along its length by seven chains of PS. Density for the main PS chain of the O-antigen is well resolved (Figure 1D) and agrees with the sequence and linkages reported for *C. crescentus* LPS (Jones et al., 2015). The O-antigen repeating unit is tightly bound to RsaA$_{NTD}$ with several interacting amino acid residues along the length of the protein (Figure 1E). The O-antigen binding pocket is stabilized by functional Ca^{2+} ions that are tightly coordinated to aspartic acid residues in RsaA$_{NTD}$ (Figure 1F), suggesting that Ca^{2+} ions are important for RsaA$_{NTD}$:PS complex assembly.

RsaA$_{NTD}$:PS Binding Is Critically Dependent on Ca^{2+} Ions

To further explore whether Ca^{2+} ions influenced the assembly of the RsaA$_{NTD}$:PS complex, we performed a desalting step to remove Ca^{2+} ions. Native MS (Gault et al., 2016) of the resulting sample showed that the RsaA$_{NTD}$:PS complex dissociated into monomers, dimers, and tetramers of RsaA$_{NTD}$ upon Ca^{2+} removal (Figures 2 and S3). Complex dissociation was reversible, and addition of Ca^{2+} resulted in complex reassembly (Figure S3B). This process of complex disassembly and reassembly could be repeated multiple times (Figure S3C). In the case of the original, assembled RsaA$_{NTD}$:PS complex, native MS showed a series of peaks corresponding to RsaA$_{NTD}$ monomers and dimers, both associated with LPS (Figure 2A), as well as a series of peaks at m/z ~12,000, which were difficult to assign (Figure 2A). Tandem MS indicated that this complex consisted of two oligomeric states, predominantly a RsaA$_{NTD}$ 21-mer, together with a 20-mer. Both oligomers bound preferentially to one unit of PS and six units of full LPS (Figure 2A; Table 1). Although we cannot rule out other PS or LPS stoichiometries, this species predominates and is validated by the cryo-EM reconstruction of the complex that showed seven sugar chains bound to 20 or 21 copies of RsaA$_{NTD}$. In line with the strong tendency to oligomerize observed in native MS, the cryo-EM structure additionally shows an extensive RsaA$_{NTD}$:RsaA$_{NTD}$ oligomerization interface in the complex. This interface is formed by salt bridges between adjoining RsaA$_{NTD}$ subunits. This binding interface is repeated around the spiral (Figures S3D–S3F), likely stabilizing the oligomeric complex.

RsaA$_{NTD}$ Binds to the O-Antigen of LPS in Two Distinct Ways

Next, we examined the biochemical basis for the O-antigen and RsaA$_{NTD}$ interaction observed in our cryo-EM structure. The repeating unit of the *C. crescentus* O-antigen contains six hexose moieties in the main PS chain: N-acetyl perosamine(PerNac)-PerNac-mannose(Man)-PerNac-PerNac-Man, with a branching 3-O-methyl glucose (Glc) on every sixth position (Jones et al., 2015). While the main PS chain was easily traceable in our map, the position of the branching Glc moiety bound to every sixth Man moiety was not immediately obvious. To help assign the position of the branching Glc in our cryo-EM map, we subjected
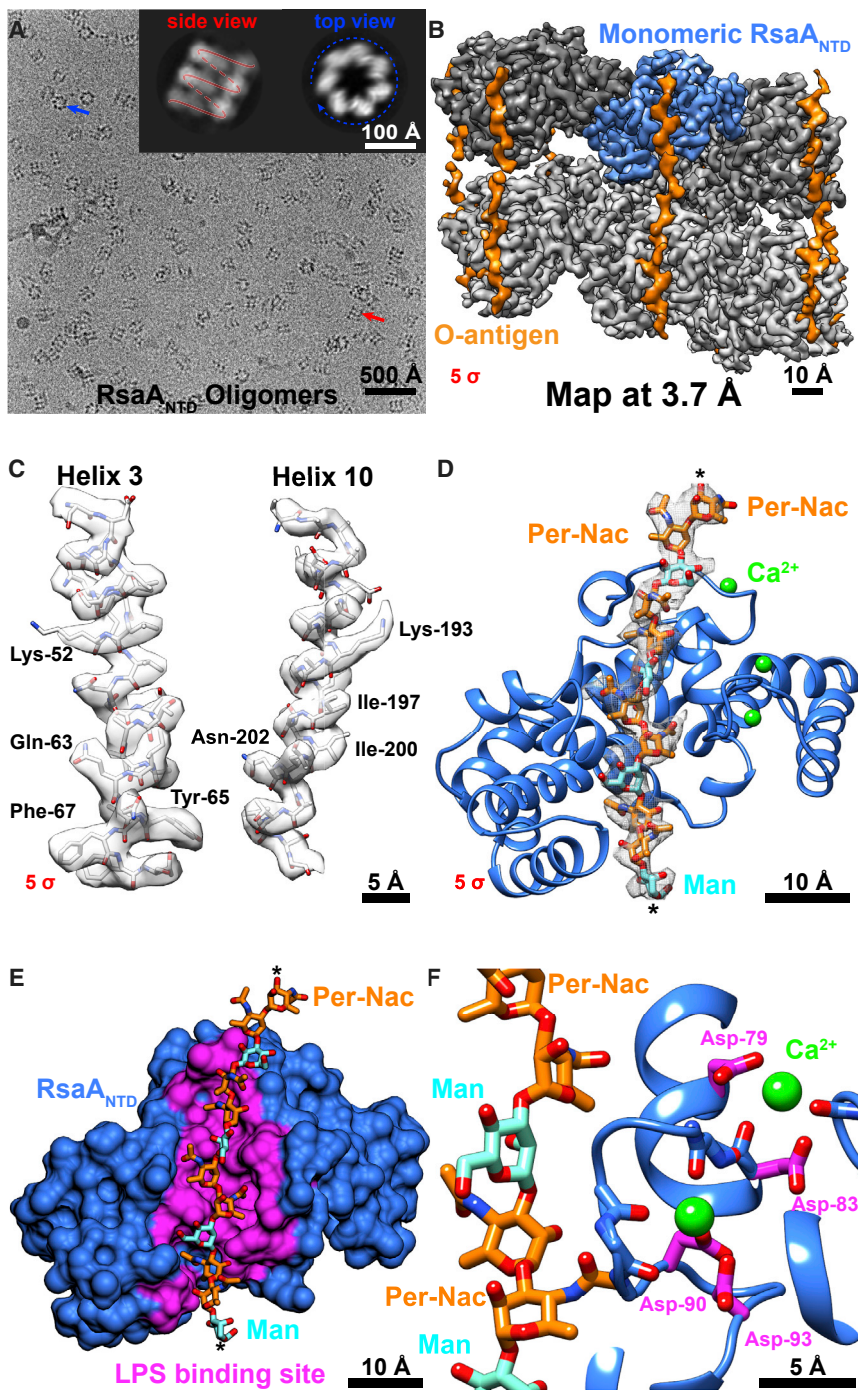
Figure 1. Cryo-EM Reconstruction of the RsaA_NTD:PS Complex at 3.7 Å Resolution

(A) Cryo-EM image of the purified complex. Inset: class averages with the spiral-like nature of the complex highlighted (see Figure S1).

(B) Density map of the complex (contour level on the lower left of panel). Different subunits are shown in different shades of gray, and density corresponding to the O-antigen of the LPS is orange (see Video S1).

(C) Regions of the map along with the built atomic model showing resolved secondary structure elements and side-chain fits. Due to the α-helical nature of the RsaA_NTD, the fit of the model to the cryo-EM map is exceptional (see Figure S2).

(D) The refined atomic model of a single RsaA_NTD subunit from the complex shown as a ribbon diagram. A stick representation of the main chain of the O-antigen is shown within the cryo-EM density. O-antigen chain is continuous along the spiral, denoted by asterisks (*).

(E) Surface representation of a single RsaA_NTD subunit showing O-antigen binding residues in magenta.

(F) Close up of two Ca^{2+} ion binding sites in relation to the O-antigen binding pocket.

a parallel simulation with Glc in positions 6 and 12 showed the same result (Figures 3C and 3F), suggesting that there might be two distinct ways that the O-antigen can bind to RsaA_NTD (Video S2). To verify this prediction from simulations with orthogonal evidence, we reinspected our cryo-EM map at lower isosurface contour levels (Figures 3G–3I), where we observed density for Glc at every third position, confirming that both states are present in our cryo-EM data and that the structure we resolved likely contains an average of both states, with seven PS chains bound in different registers to the RsaA_NTD spiral.

Another noteworthy observation from the MD simulations was that all three Ca^{2+} ions in the structure remain tightly and stably bound to RsaA_NTD throughout the simulations, consistent with our biochemical and native MS data (Figure 2). In fact, the entire Ca^{2+}-binding loop consisting of RsaA amino acid residues 77–100 were significantly stabilized when

monomeric RsaA_NTD with two repeats of the O-antigen resolved in our structure to MD simulations. Simulations in the absence of branching Glc moieties showed large root mean square fluctuations (RMSFs) for both the sugar and the protein atoms (Figures 3A, 3D, and S4). On the inclusion of the Glc moiety in positions 3 and 9, these fluctuations were dramatically reduced and showed the core of the repeating sugar locked to its binding pocket within the RsaA_NTD fold (Figures 3B and 3E). Surprisingly,

the branching Glc moieties of the O-antigen were included in the simulations (Figures S4J–S4L), suggesting that Ca^{2+} and LPS binding are linked with each other (Figure S4M) and augment complex assembly in a cooperative manner.

RsaA Binds the Entire Length of the O-Antigen on Cells

Next, we tested whether our *in vitro* results could be replicated on cells. A density for both RsaA_NTD as well as RsaA_CTD is
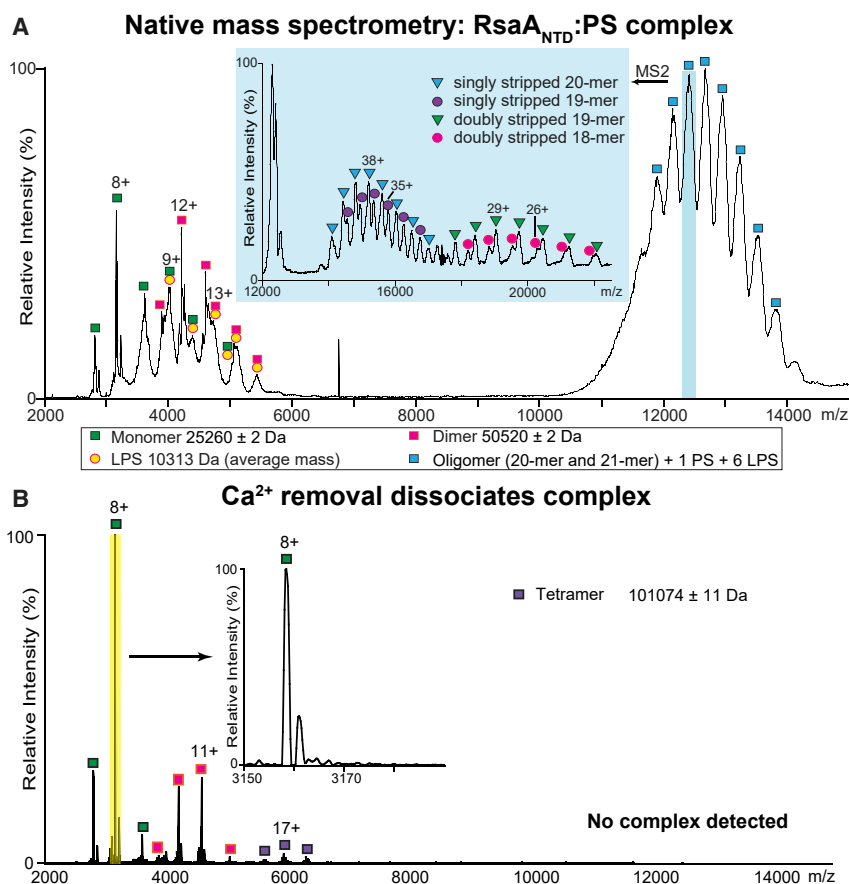
A. Native mass spectrometry: RsaA_NTD:PS complex

Legend:
- singly stripped 20-mer
- singly stripped 19-mer
- doubly stripped 19-mer
- doubly stripped 18-mer

MS2

- Monomer 25260 ± 2 Da
- Dimer 50520 ± 2 Da
- LPS 10313 Da (average mass)
- Oligomer (20-mer and 21-mer) + 1 PS + 6 LPS

B. Ca²⁺ removal dissociates complex

- Tetramer 101074 ± 11 Da

No complex detected

Figure 2. Deducing Protein:Sugar Stoichiometry and Ca²⁺-Dependent Assembly Using High-Resolution Native MS

(A) Native mass spectrum of purified RsaA_NTD:PS complexes show populations of monomer and dimer, both associated with LPS (average mass 10313 Da) and oligomers (20-mer and 21-mer) bound to one unit of PS and six units of LPS. Inset: High energy MS/MS of the oligomeric RsaA_NTD performed by isolating the peak at ~12404 m/z and dissociating at a voltage of 220V applied to the higher-energy collisional dissociation (HCD) cell. The inset spectrum (blue background) shows stripped oligomers generated by loss of single subunits from the parent complex (21-mer→20-mer→19-mer) and (20-mer→19-mer→18-mer) allowing us to conclude that the original oligomer consists predominantly of a 21-mer and a 20-mer with one unit of PS and six units of LPS each (see Table 1), although other LPS or PS hydrolysis products may also be present.

(B) Mass spectrum of the RsaA_NTD:PS sample after Ca²⁺ removal shows presence of RsaA_NTD monomers, dimers, and tetramers only (see also Figure S3).

OM like the native S-layer, we observed three density layers proximal to the OM (Figures 4E and 4F). These density layers had the same appearance and spacing as those seen in side views of our cryo-EM structure of the RsaA_NTD:PS complex (Figure 4F, inset). This showed that not only can RsaA_NTD bind to cellular LPS but also that binding occurs all along the LPS O-antigen due to its repeating nature. Similar results were obtained on the addition of full-length RsaA, where three density layers were observed on top of a RsaA_CTD layer (Figure S5). Also consistent with our biochemical data, when Ca²⁺ ions were depleted from the reaction by the addition of EGTA (ethylene glycol-bis(β-aminoethyl ether)-N,N,N′,N′-tetraacetic acid) and RsaA_NTD was added to ΔrsaA cells (Figure S5H), no

seen in raw electron cryotomograms of *C. crescentus* cell stalks (Figure 4A) and also in subtomogram averages produced from the surface of these stalks (Figure 4B). Density layers for RsaA domains are absent in a ΔrsaA mutant, which does not possess an S-layer (Figures 4C and 4D). To test whether RsaA_NTD would also bind to cellular LPS, we added purified RsaA_NTD to ΔrsaA cells. Instead of forming a single layer of density outside the

Table 1. Expected and Measured Masses of RsaA_NTD Detected in Native MS

Subunit/Complex	Expected Mass (Da)	Measured Mass (Da)	Mass Difference (Da)	Mass Difference (%)
Monomer[a]	25261	25260 ± 2	1	0.003958671
Dimer	50522	50520 ± 2	2	0.003958671
Monomer + LPS (Jones et al., 2015; Smit et al., 2008)	35644.51	35549 ± 519	95.51	0.267951502
Dimer + LPS	60905.51	60857 ± 918	48.51	0.079647966
Singly stripped 20-mer + 1 PS + 6 LPS	577382.22[b]	577492 ± 414	109.78	0.019013402
Singly stripped 19-mer + 1 PS + 6 LPS	552055.22[b]	552599 ± 400	543.78	0.098501016
Doubly stripped 19-mer + 1 PS + 6 LPS	552055.22[b]	552317 ± 190	261.78	0.047419169
Doubly stripped 18-mer + 1 PS + 6 LPS	526728.22[b]	527661 ± 442	932.78	0.17708943

[a]Residues 2–250 and the amino acids Glu-Asn of the genetically engineered TEV protease site.
[b]Salt adducts (Na⁺/Ca²⁺) were observed bound to each monomer (average mass of 66 Da per monomer) and were therefore included when we calculated the expected mass of the stripped oligomers. The expected mass of LPS is 10383.51 Da and the expected mass of PS is 8541.16 Da according to the structure of LPS of *C. crescentus* reported in a previous study (Jones, 2015).
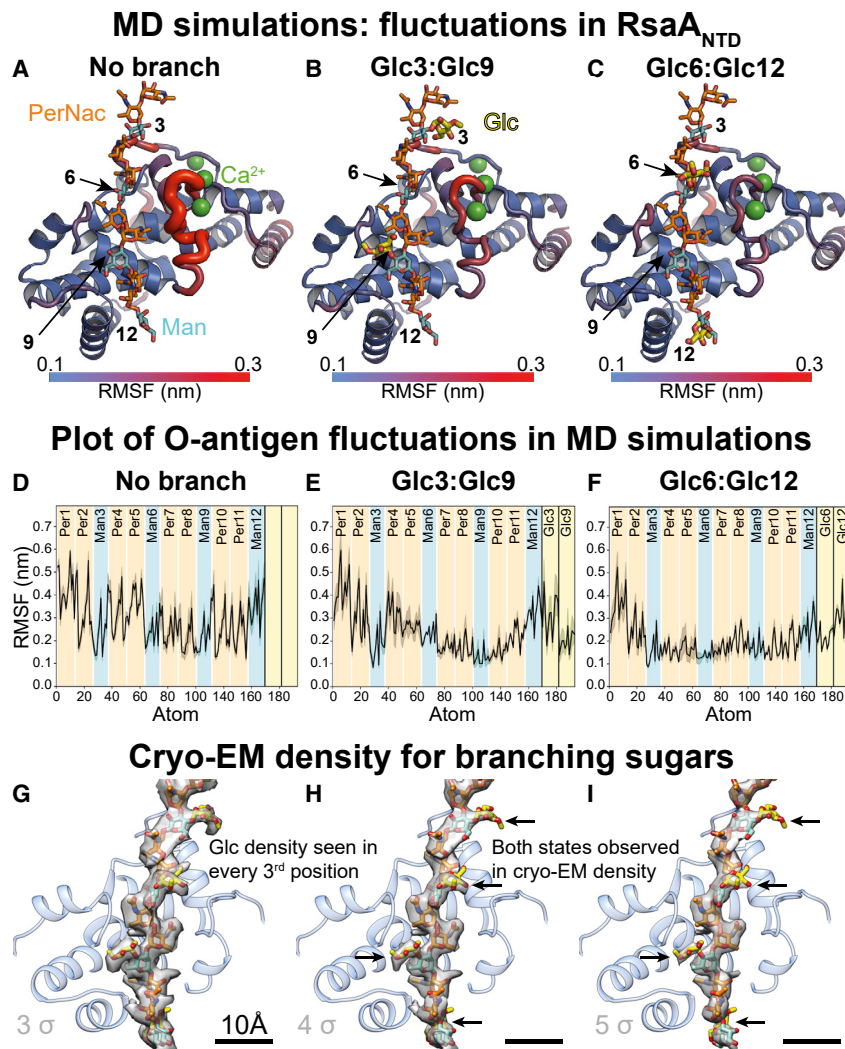
MD simulations: fluctuations in RsaA$_{NTD}$

A No branch   **B** Glc3:Glc9   **C** Glc6:Glc12

Plot of O-antigen fluctuations in MD simulations

D No branch   **E** Glc3:Glc9   **F** Glc6:Glc12

Cryo-EM density for branching sugars

G Glc density seen in every 3rd position   **H** Both states observed in cryo-EM density   **I**

3 σ   10Å   4 σ   5 σ

Figure 3. Probing RsaA$_{NTD}$ Binding to the O-Antigen of LPS Using MD Simulations

(A) MD simulation of RsaA$_{NTD}$ bound to the O-antigen with no branching sugar moieties.

(B) Simulation of RsaA$_{NTD}$ bound to the O-antigen with 3-O-methyl-glucose (Glc) moieties at positions 3 and 9.

(C) Simulation of RsaA$_{NTD}$ bound to the O-antigen with Glc moieties at positions 6 and 12.

(D) Plot of RMSF of the O-antigen atoms in the MD simulation presented in (A).

(E) Plot of RMSF of the O-antigen atoms in the MD simulation presented in (B).

(F) Plot of RMSF of the O-antigen atoms in the MD simulation presented in (C).

(G–I) Cryo-EM density at different isosurface contour levels showing density for the branching sugar moieties at every third position (see Figure S4)

of the S-layer lattice directly on the surface of cell stalks (Figure S6). The subtomogram averaging map shows large anisotropy in resolution, with the resolution highest in RsaA$_{NTD}$, close to the 6-fold symmetrization axis (Figure S6B). Both the RsaA$_{NTD}$ cryo-EM structure as well as the RsaA$_{CTD}$ X-ray structure (Bharat et al., 2017) could be docked into the cryo-ET density unambiguously as rigid bodies (Figures 5A and 5B; Video S3). All α helices of RsaA$_{NTD}$ are resolved in the cryo-ET map (Figure 5C), and large side chains are resolved, which fit the density well without any further refinement (Figure 5D). Satisfyingly, a clear density for the O-antigen of the LPS is observed in the same relative location as in the single-particle cryo-EM map of the RsaA$_{NTD}$:PS complex (Figure 5E). It is worth mentioning that the RsaA$_{NTD}$:RsaA$_{NTD}$ interface is almost unchanged from the interaction observed in the RsaA$_{NTD}$:PS spiral complex (Figures 1 and S3D–S3F). This observation suggests that the planar hexameric arrangement of RsaA$_{NTD}$ in the native S-layer is at least partially imposed by the hexagonal symmetry of the RsaA$_{CTD}$ outer lattice.

There are very few contact sites observed between RsaA$_{NTD}$ and RsaA$_{CTD}$ (Video S4), showing why the two domains can oligomerize independently. The two domains are connected by a short linker region, which appears as a smeared density in the cryo-ET map, suggesting some flexibility (Figures S6D–S6F; Video S4). The density for the LPS O-antigen is clearly resolved near the RsaA$_{NTD}$ domain, and this density ends within the RsaA$_{NTD}$ layer and does not extend outward to the RsaA$_{CTD}$ (Figure 5G). This indicates that upon secretion and assembly into an S-layer, RsaA proteins localize at the very tip of the O-antigen. These observations are consistent with the fact that antibodies against the O-antigen are unable to stain the O-antigen when the S-layer is present (Walker et al., 1994).

S-layer assembly or decoration of the cellular LPS in the OM was observed, in line with the desalting experiments conducted in native MS.

In light of these *in situ* results, together with the stoichiometry of the RsaA$_{NTD}$:PS complex observed in cryo-EM and confirmed by native MS in which 20 or 21 monomers of RsaA$_{NTD}$ were observed in the complex bound to seven O-antigen molecules, we predict using the total mass of the complex that the full RsaA$_{NTD}$ spiral would bind on average 294 hexose moieties, which allows us to calculate that there are 42 hexose moieties in the cellular O-antigen of the native *C. crescentus*. This calculation is also consistent with the distances measured between the OM and the S-layer in our cryo-ET data (Figure 4), accounting for the size of the core OS proximal to the OM.

Near-Atomic Resolution *In Situ* Structure of the *C. crescentus* S-Layer

To obtain a more detailed view of the cellular S-layer, we used recently described subtomogram averaging algorithms (Turoňová et al., 2017) to obtain a 4.8 Å resolution structure

Cryo-ET slice through cellular stalk

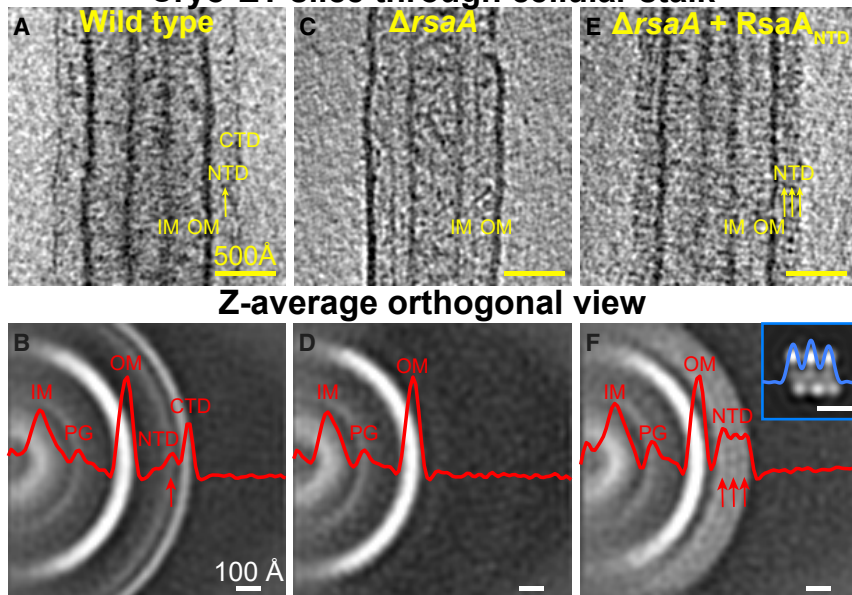## Z-average orthogonal view

Figure 4. Binding of RsaA$_{NTD}$ to Cellular LPS Occurs along the Entire Length of the O-Antigen

(A) Cryo-ET slice through a cellular stalk of CB15N *C. crescentus*. An assembled S-layer is observed, with RsaA$_{NTD}$ and RsaA$_{CTD}$ layers ~180 Å and ~230 Å away from the OM, respectively.

(B) Subtomogram averaging of the stalk shows clear densities for the OM, RsaA$_{NTD}$, and RsaA$_{CTD}$.

(C) Slice through a stalk lacking RsaA (Δ*rsaA*).

(D) Corresponding subtomogram average from Δ*rsaA* stalks.

(E) Slice through a Δ*rsaA* cellular stalk with exogenous RsaA$_{NTD}$ added.

(F) Corresponding subtomogram average shows three density layers on the outside of the OM. Inset: Side view of the RsaA$_{NTD}$:PS cryo-EM structure also shows three layers of protein bound to the O-antigen PS with the same spacing (see Figure S5).

In the other direction toward the cell, at low contour levels, the O-antigen density extends down toward the OM and is probably formed of flexible and fluctuating O-antigen repeats connected to the core OS (Figure 5F; Video S5). The relative distance between the S-layer and the OM remains constant over the cell body and stalks (Figure S7), showing that the length of the LPS O-antigen is the same all around the cell. Furthermore, the S-layer arrangement including the near-hexagonal symmetry is also seen over the cell body (Figure S7). Therefore, the near-atomic resolution *in situ* structure of the *C. crescentus* S-layer allows positioning of not only the two RsaA domains but also the O-antigen of LPS relative to the OM of the bacterial cell (Figure 5H), providing an atomic resolution snapshot of the outermost layer of *C. crescentus* bacteria made up of protein and polysaccharide.

DISCUSSION

One of the outstanding goals of structural biology is to resolve atomic resolution cellular structures and to study cellular processes in atomic detail *in situ*. To this end on the technical side, this study demonstrates how cryo-ET and subtomogram averaging (4.8 Å cellular S-layer) is closing the gap to single-particle cryo-EM (3.7 Å RsaA$_{NTD}$:PS complex) and X-ray crystallography (2.7 Å RsaA$_{CTD}$). Modern cryo-ET imaging can provide molecular resolution insights into the architecture and organization of cells (Chang et al., 2016; Mahamid et al., 2016). Here we used cryo-ET combined with subtomogram averaging to reveal a repeated cellular structure at near-atomic resolution, allowing the fundamental biological process of S-layer assembly to be studied directly in its cellular context (Figure 5H).

Our structure of the complete *C. crescentus* S-layer, together with the O-antigen of the LPS, is a potential target for synthetic

biology applications, in which tagged S-layers could be used to link genotype to protein displayed at high copy numbers on surfaces. The first such technical application, developed using the X-ray structure of RsaA$_{CTD}$ has been recently reported (Charrier et al., 2019).

Our structure of the RsaA$_{NTD}$:PS complex confirms previous studies that showed that the N-terminal residues of RsaA are critical for S-layer anchoring (Ford et al., 2007). A majority of the mutations in RsaA$_{NTD}$, including amino acid exchanges or insertions before position 225 in the amino acid sequence, lead to complete loss of S-layer anchoring (Ford et al., 2007), consistent with the extensive interaction observed between the O-antigen and RsaA$_{NTD}$ in our cryo-EM structure (Figures S4A–S4C). Our integrated structural biology approach has technical implications to the future structural studies of LPS. LPS is nearly ubiquitous in Gram-negative bacteria, and it is found in several important human pathogens. LPS assembly and biogenesis has thus rightly been the focus of several prominent structural biology efforts in the recent past, for example Bi et al., 2018 and Caffalette et al., 2019, to name a few. Here we show that by combining cryo-EM and cryo-ET with native MS, it is possible to understand not only the biochemistry but also the cellular architecture and arrangement of LPS, revealing how LPS molecules are located in the space directly outside Gram-negative *C. crescentus* cells. Using a similar integrated approach of combining EM with MS, LPS molecules in other bacteria may be studied, allowing molecular details of this enigmatic molecule to be revealed.

In *C. crescentus*, future genetic and biochemical studies that mutate and perturb the LPS O-antigen might shed light onto how LPS biogenesis and secretion is coupled with S-layer assembly. Only density for the LPS O-antigen bound to RsaA$_{NTD}$ was resolved in our cryo-EM map; therefore it is still not completely clear how the core oligosaccharide and lipid A of the LPS is arranged on cells. Further structural and cell biology studies in the *C. crescentus* system will be required to understand how the LPS is anchored at the other end, away from the S-layer by the bacterial OM.
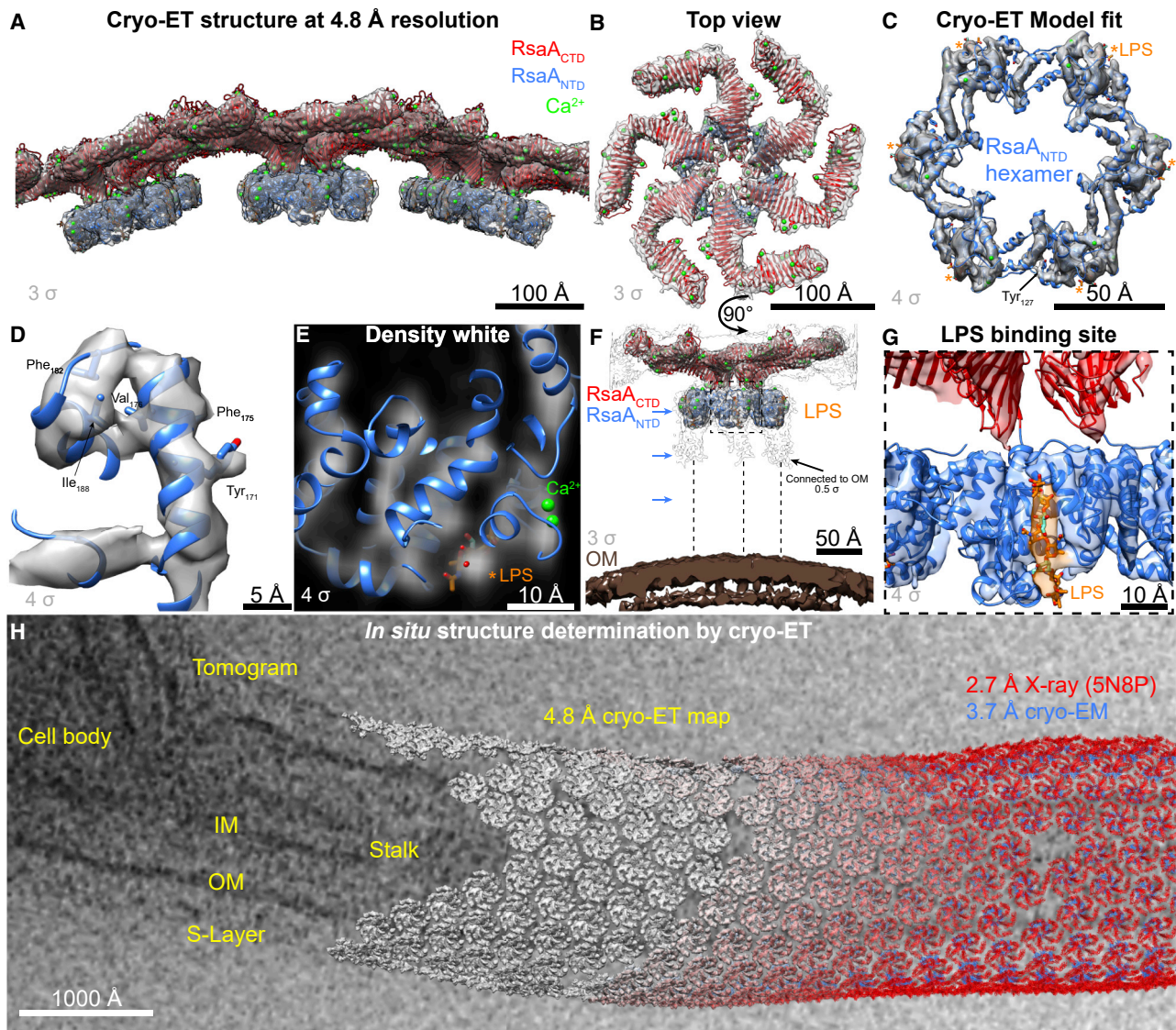
Figure 5. *In Situ* Cryo-ET of the Native *C. crescentus* S-Layer at 4.8 Å Resolution

(A) Subtomogram averaging at 4.8 Å resolution of the native S-layer from cell stalks. RsaA_CTD X-ray structure (PDB: 5N8P, red ribbon) and RsaA_NTD cryo-EM structure (blue ribbon) are docked into the density (contour level shown on lower left of each panel, see Figure S6).

(B) Top View of a Single Hexameric Unit

(C) Six subunits of the cryo-EM structure of RsaA_NTD docked into the cryo-ET map. LPS densities highlighted with asterisks (*).

(D) A closeup of a single RsaA_NTD α-helix showing some resolved bulky side chains in the cryo-ET map.

(E) A ribbon diagram of one RsaA_NTD subunit overlaid on a slice through the cryo-ET map. A clear density for the O-antigen is observed at the same relative location as in the cryo-EM RsaA_NTD:PS structure.

(F) A side view of a single hexamer is shown relative to the OM of the cell. Densities of O-antigen bound to RsaA extend downward to the OM (black outline density). Positions of RsaA_NTD:PS density layers as seen in Figure 4F are highlighted with blue arrows (see Video S3).

(G) A closeup view of the O-antigen binding pocket resolved in the cryo-ET map.

(H) Cellular structural biology from cells to atoms. Tomographic slice of a *C. crescentus* cell. Copies of the 4.8 Å cryo-ET structure are overlaid on the tomographic slice at their refined cellular locations. Atomic structures determined by X-ray crystallography (RsaA_CTD 2.7 Å) and cryo-EM (RsaA_NTD 3.7 Å) are docked into the cryo-ET map (see Video S5).

It is reasonable to expect that newly secreted RsaA proteins might be guided toward the S-layer lattice along O-antigen chains via binding to RsaA_NTD (Figure 6). O-antigen binding is Ca^{2+} dependent (Video S4), and Ca^{2+} levels are higher in the extracellular space (Baines et al., 2000; Jeziorski et al., 2008),

enough to trigger spontaneous S-layer assembly (Herrmann et al., 2017). RsaA_NTD can bind along the entire length of the O-antigen of the cellular LPS (Figures 6B and S5), consistent with the multiple binding modes observed in our cryo-EM structure and confirmed by MD simulations. When full-length RsaA
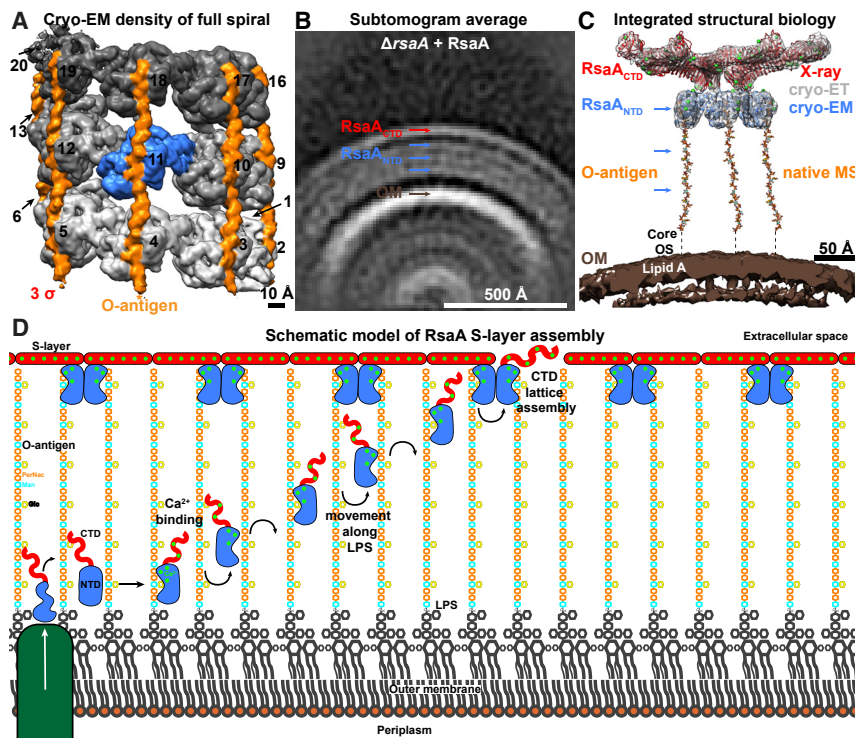
Figure 6. Schematic Model of *C. crescentus* S-Layer Assembly on the Cell Surface

(A) Density of the cryo-EM structure of the isolated RsaA$_{NTD}$:PS complex contoured at 3 σ away from the mean. The reconstruction of the entire spiral is shown, no mask applied (3.9 Å resolution map). RsaA$_{NTD}$ subunits are shown in different shades of gray (additionally numbered), and density corresponding to the O-antigen of the LPS is shown in orange. Asterisk (*) denotes density for LPS extending at lower contour levels only in one direction.

(B) Subtomogram averaging of the sample with exogenous added full-length RsaA to cells lacking native S-layer (ΔrsaA) demonstrates that full-length RsaA can bind along the entire length of the O-antigen and can form a partly assembled outer lattice (panel same as Figure S5G). We expect that only RsaA molecules at the tip of the O-antigen are able to partially assemble the outer lattice because of steric hindrance by a mesh of LPS in the layers below.

(C) Using a combined structural approach, X-ray crystallography (RsaA$_{CTD}$, PDB: 5N8P, red), cryo-EM (RsaA$_{NTD}$, blue), cryo-ET (subtomogram average, gray), and native MS (O-antigen, orange), we report a model of a full bacterial S-layer bound to LPS.

(D) Schematic model of *C. crescentus* S-layer assembly. RsaA is secreted to the extracellular milieu, where RsaA binds to Ca^{2+} and LPS. This binding has been observed in our cryo-EM structure of the RsaA$_{NTD}$:PS complex (Figure 1) and verified by native MS (Figure 2). Next, RsaA is guided on LPS molecules by binding to the O-antigen along multiple sites, as observed in our cryo-EM structure (Figure 1), confirmed by MD simulations (Figures 3 and S4) as well as by *in situ* experiments showing binding of RsaA along the entire length of the LPS O-antigen (Figure 4). RsaA molecules are unable to assemble into an S-layer lattice near the OM (Figure S5), likely due to steric hindrance by a meshwork of LPS molecules. At the tips of the LPS O-antigen, whose length we accurately estimated using native MS (Figure 2), RsaA molecules can bind with a pre-existing S-layer to complete gaps in the lattice via oligomerization through RsaA$_{CTD}$ (B and Bharat et al., 2017).

was added to a *C. crescentus* strain lacking an S-layer, formation of an additional (fourth) density layer at the same distance from the OM as the native RsaA$_{CTD}$ layer was observed, suggesting that RsaA molecules bound at the ends of the LPS had at least partially assembled into an S-layer lattice. This indicates that lattice assembly is only possible when RsaA is bound at the tip of the O-antigen, implying that a meshwork of LPS and other molecules might sterically hinder premature S-layer formation.

RsaA$_{NTD}$ domains in the assembled S-layer are attached to the end of the LPS (Figure 6C), and RsaA$_{CTD}$ domains oligomerise in a Ca^{2+}-dependent manner to form the outer S-layer lattice (Figures 6C and 5H; Video S5). Overall, both RsaA$_{NTD}$ and RsaA$_{CTD}$ contain several functionally important Ca^{2+} ions, which have roles in LPS binding as well as lattice assembly. Consistent with this strong Ca^{2+} dependence, cooperative assembly is observed in both RsaA domains, allowing this remarkable two-dimensional array to be assembled on the surface of *C. crescentus* cells (Figure 6D). It is interesting to note that Ca^{2+}-dependence has been previously described for other unrelated S-layers from Gram-positive bacteria (Baranova et al., 2012) and archaea (Sumper et al., 1990), perhaps suggesting similar mechanisms of assembly. However, further work will be needed to verify this expectation. In the case of the *C. crescentus* S-layer, it is remarkable how division of labor between different RsaA domains, where RsaA$_{NTD}$ mediates cell anchoring and RsaA$_{CTD}$ forms the lattice layer, allows this remarkable polyprotein to perform multiple tasks on the cell surface to form micron-scale, two-dimensional sheaths on membranes with variable curvature.

Finally, fluorescently tagged S-layers derived from our structure will open the door to studying S-layer dynamics (Charrier et al., 2019; Comerci et al., 2019) with respect to the cell cycle and cell morphogenesis. A recent optical microscopy study on the same system has shown that a new *C. crescentus* S-layer is inserted at the mid-cell or at the cell poles (Comerci et al., 2019). In the light of this spatiotemporal regulation of S-layer morphogenesis, it seems remarkable how molecular rearrangements within the cell control biogenesis and assembly of a two-dimensional lattice 180 Å away from the OM, mediated by long rope-like LPS molecules. Future structural and cell biology studies on this system will reveal how S-layer morphogenesis is coupled with critical cellular processes such as cell elongation, peptidoglycan synthesis, LPS biogenesis, LPS secretion, and cell division, providing insights into the mechanism of how spatial information is relayed from the cytoplasm to the extracellular environment of the cell.

STAR★METHODS

Detailed methods are provided in the online version of this paper and include the following:

- KEY RESOURCES TABLE
- LEAD CONTACT AND MATERIALS AVAILABILITY

SUPPLEMENTAL INFORMATION

Supplemental Information can be found online at https://doi.org/10.1016/j.cell.2019.12.006.

AUTHOR CONTRIBUTIONS

A.V.K., P.J.S., and T.A.M.B. designed research; A.V.K, H.T., G.G.H., D.K.-C., P.J.S., and T.A.M.B. performed experiments; A.V.K., H.T., Y.V.B., P.J.S., C.V.R., and T.A.M.B. analyzed data; A.V.K. and T.A.M.B. wrote the manuscript with the support of all authors.

DECLARATION OF INTERESTS

The authors declare no competing interests.

REFERENCES

Abraham, M.J., Murtola, T., Schulz, R., Páll, S., Smith, J.C., Hess, B., and Lindahl, E. (2015). GROMACS: High performance molecular simulations through multi-level parallelism from laptops to supercomputers. SoftwareX *1-2*, 19–25.

Adams, P.D., Afonine, P.V., Bunkóczi, G., Chen, V.B., Davis, I.W., Echols, N., Headd, J.J., Hung, L.-W., Kapral, G.J., Grosse-Kunstleve, R.W., et al. (2010). PHENIX: a comprehensive Python-based system for macromolecular structure solution. Acta Crystallogr. D Biol. Crystallogr. *66*, 213–221.

Albers, S.V., and Meyer, B.H. (2011). The archaeal cell envelope. Nat. Rev. Microbiol. *9*, 414–426.

Arbing, M.A., Chan, S., Shin, A., Phan, T., Ahn, C.J., Rohlin, L., and Gunsalus, R.P. (2012). Structure of the surface layer of the methanogenic archaean *Methanosarcina acetivorans*. Proc. Natl. Acad. Sci. USA *109*, 11812–11817.

Baines, S.B., Webster, K.E., Kratz, T.K., Carpenter, S.R., and Magnuson, J.J. (2000). Synchronous behavior of temperature, calcium, and chlorophyll in lakes of northern Wisconsin. Ecology *81*, 815–825.

Baranova, E., Fronzes, R., Garcia-Pino, A., Van Gerven, N., Papapostolou, D., Péhau-Arnaudet, G., Pardon, E., Steyaert, J., Howorka, S., and Remaut, H. (2012). SbsB structure and lattice reconstruction unveil Ca2+ triggered S-layer assembly. Nature *487*, 119–122.

Bharat, T.A.M., and Scheres, S.H.W. (2016). Resolving macromolecular structures from electron cryo-tomography data using subtomogram averaging in RELION. Nat. Protoc. *11*, 2054–2065.

Bharat, T.A.M., Riches, J.D., Kolesnikova, L., Welsch, S., Krähling, V., Davey, N., Parsy, M.-L., Becker, S., and Briggs, J.A.G. (2011). Cryo-electron tomography of Marburg virus particles and their morphogenesis within infected cells. PLoS Biol. *9*, e1001196.

Bharat, T.A.M., Russo, C.J., Löwe, J., Passmore, L.A., and Scheres, S.H.W. (2015). Advances in Single-Particle Electron Cryomicroscopy Structure Determination applied to Sub-tomogram Averaging. Structure *23*, 1743–1753.

Bharat, T.A.M., Kureisaite-Ciziene, D., Hardy, G.G., Yu, E.W., Devant, J.M., Hagen, W.J.H., Brun, Y.V., Briggs, J.A.G., and Löwe, J. (2017). Structure of the hexagonal surface layer on *Caulobacter crescentus* cells. Nat. Microbiol. *2*, 17059.

Bi, Y., Mann, E., Whitfield, C., and Zimmer, J. (2018). Architecture of a channel-forming O-antigen polysaccharide ABC transporter. Nature *553*, 361–365.

Burnley, T., Palmer, C.M., and Winn, M. (2017). Recent developments in the CCP-EM software suite. Acta Crystallogr. D Struct. Biol. *73*, 469–477.

Bussi, G., Donadio, D., and Parrinello, M. (2007). Canonical sampling through velocity rescaling. J. Chem. Phys. *126*, 014101.

Cabeen, M.T., Murolo, M.A., Briegel, A., Bui, N.K., Vollmer, W., Ausmees, N., Jensen, G.J., and Jacobs-Wagner, C. (2010). Mutations in the Lipopolysaccharide biosynthesis pathway interfere with crescentin-mediated cell curvature in *Caulobacter crescentus*. J. Bacteriol. *192*, 3368–3378.

Caffalette, C.A., Corey, R.A., Sansom, M.S.P., Stansfeld, P.J., and Zimmer, J. (2019). A lipid gating mechanism for the channel-forming O antigen ABC transporter. Nat. Commun. *10*, 824.

Chang, Y.-W., Rettberg, L.A., Treuner-Lange, A., Iwasa, J., Søgaard-Andersen, L., and Jensen, G.J. (2016). Architecture of the type IVa pilus machine. Science *351*, aad2001.

Charrier, M., Li, D., Mann, V., Yun, L., Jani, S., Rad, B., Cohen, B.E., Ashby, P.D., Ryan, K., and Ajo-Franklin, C.M. (2019). Engineering the S-layer of Caulobacter crescentus as a Foundation for Stable, High-Density, 2D Living Materials. ACS Synth. Biol. *8*, 181–190.

Comerci, C.J., Herrmann, J., Yoon, J., Jabbarpour, F., Zhou, X., Nomellini, J.F., Smit, J., Shapiro, L., Wakatsuki, S., and Moerner, W.E. (2019). Topologically-guided continuous protein crystallization controls bacterial surface layer self-assembly. Nat. Commun. *10*, 2731.

Darden, T., York, D., and Pedersen, L. (1993). Particle mesh Ewald - an N.log(N) method for Ewald sums in large systems. J. Chem. Phys. *98*, 10089–10092.

Dong, H., Xiang, Q., Gu, Y., Wang, Z., Paterson, N.G., Stansfeld, P.J., He, C., Zhang, Y., Wang, W., and Dong, C. (2014). Structural basis for outer membrane lipopolysaccharide insertion. Nature *511*, 52–56.

Emsley, P., Lohkamp, B., Scott, W.G., and Cowtan, K. (2010). Features and development of Coot. Acta Crystallogr. D Biol. Crystallogr. *66*, 486–501.

Evinger, M., and Agabian, N. (1977). Envelope-associated nucleoid from *Caulobacter crescentus* stalked and swarmer cells. J. Bacteriol. *132*, 294–301.

Fagan, R.P., and Fairweather, N.F. (2014). Biogenesis and functions of bacterial S-layers. Nat. Rev. Microbiol. *12*, 211–222.

Ford, M.J., Nomellini, J.F., and Smit, J. (2007). S-layer anchoring and localization of an S-layer-associated protease in *Caulobacter crescentus*. J. Bacteriol. *189*, 2226–2237.

Gault, J., Donlan, J.A.C., Liko, I., Hopper, J.T.S., Gupta, K., Housden, N.G., Struwe, W.B., Marty, M.T., Mize, T., Bechara, C., et al. (2016). High-resolution mass spectrometry of small molecules bound to membrane proteins. Nat. Methods *13*, 333–336.

Gonin, M., Quardokus, E.M., O'Donnol, D., Maddock, J., and Brun, Y.V. (2000). Regulation of stalk elongation by phosphate in *Caulobacter crescentus*. J. Bacteriol. *182*, 337–347.

Hagen, W.J.H., Wan, W., and Briggs, J.A.G. (2017). Implementation of a cryo-electron tomography tilt-scheme optimized for high resolution subtomogram averaging. J. Struct. Biol. *197*, 191–198.

Hardy, G.G., Allen, R.C., Toh, E., Long, M., Brown, P.J.B., Cole-Tobian, J.L., and Brun, Y.V. (2010). A localized multimeric anchor attaches the Caulobacter holdfast to the cell pole. Mol. Microbiol. *76*, 409–427.

Herrmann, J., Jabbarpour, F., Bargar, P.G., Nomellini, J.F., Li, P.N., Lane, T.J., Weiss, T.M., Smit, J., Shapiro, L., and Wakatsuki, S. (2017). Environmental Calcium Controls Alternate Physical States of the Caulobacter Surface Layer. Biophys. J. *112*, 1841–1851.

Houwink, A.L. (1953). A macromolecular mono-layer in the cell wall of *Spirillum* spec. Biochim. Biophys. Acta *10*, 360–366.

Huang, J., Rauscher, S., Nawrocki, G., Ran, T., Feig, M., de Groot, B.L., Grubmüller, H., and MacKerell, A.D., Jr. (2017). CHARMM36m: an improved force field for folded and intrinsically disordered proteins. Nat. Methods *14*, 71–73.

Jeziorski, A., Yan, N.D., Paterson, A.M., Desellas, A.M., Turner, M.A., Jeffries, D.S., Keller, B., Weeber, R.C., McNicol, D.K., Palmer, M.E., et al. (2008). The widespread threat of calcium decline in fresh waters. Science *322*, 1374–1377.

Jones, M.D. (2015). Studies on the structure and composition of the outer membrane of *Caulobacter crescentus*. PhD thesis (The University of British Columbia).

Jones, M.D., Vinogradov, E., Nomellini, J.F., and Smit, J. (2015). The core and O-polysaccharide structure of the *Caulobacter crescentus* lipopolysaccharide. Carbohydr. Res. *402*, 111–117.

Kim, S., Lee, J., Jo, S., Brooks, C.L., 3rd, Lee, H.S., and Im, W. (2017). CHARMM-GUI ligand reader and modeler for CHARMM force field generation of small molecules. J. Comput. Chem. *38*, 1879–1886.

Kremer, J.R., Mastronarde, D.N., and McIntosh, J.R. (1996). Computer visualization of three-dimensional image data using IMOD. J. Struct. Biol. *116*, 71–76.

Lee, J., Cheng, X., Swails, J.M., Yeom, M.S., Eastman, P.K., Lemkul, J.A., Wei, S., Buckner, J., Jeong, J.C., Qi, Y., et al. (2016). CHARMM-GUI Input Generator for NAMD, GROMACS, AMBER, OpenMM, and CHARMM/OpenMM Simulations Using the CHARMM36 Additive Force Field. J. Chem. Theory Comput. *12*, 405–413.

Li, Y., Orlando, B.J., and Liao, M. (2019). Structural basis of lipopolysaccharide extraction by the LptB$_2$FGC complex. Nature *567*, 486–490.

Lupas, A., Engelhardt, H., Peters, J., Santarius, U., Volker, S., and Baumeister, W. (1994). Domain structure of the *Acetogenium kivui* surface layer re-vealed by electron crystallography and sequence analysis. J. Bacteriol. *176*, 1224–1233.

Mahamid, J., Pfeffer, S., Schaffer, M., Villa, E., Danev, R., Cuellar, L.K., Förster, F., Hyman, A.A., Plitzko, J.M., and Baumeister, W. (2016). Visualizing the molecular sociology at the HeLa cell nuclear periphery. Science *351*, 969–972.

Mastronarde, D.N. (2005). Automated electron microscope tomography using robust prediction of specimen movements. J. Struct. Biol. *152*, 36–51.

Murshudov, G.N., Skubák, P., Lebedev, A.A., Pannu, N.S., Steiner, R.A., Nicholls, R.A., Winn, M.D., Long, F., and Vagin, A.A. (2011). REFMAC5 for the refinement of macromolecular crystal structures. Acta Crystallogr. D Biol. Crystallogr. *67*, 355–367.

Owens, T.W., Taylor, R.J., Pahil, K.S., Bertani, B.R., Ruiz, N., Kruse, A.C., and Kahne, D. (2019). Structural basis of unidirectional export of lipopolysaccharide to the cell surface. Nature *567*, 550–553.

Parrinello, M., and Rahman, A. (1981). Polymorphic transitions in single crystals: A new molecular-dynamics method. J. Appl. Physiol. *52*, 7182–7190.

Pettersen, E.F., Goddard, T.D., Huang, C.C., Couch, G.S., Greenblatt, D.M., Meng, E.C., and Ferrin, T.E. (2004). UCSF Chimera–a visualization system for exploratory research and analysis. J. Comput. Chem. *25*, 1605–1612.

Poindexter, J.S. (1964). Biological properties and classification of the *Caulobacter* group. Bacteriol. Rev. *28*, 231–295.

Pum, D., Toca-Herrera, J.L., and Sleytr, U.B. (2013). S-layer protein self-assembly. Int. J. Mol. Sci. *14*, 2484–2501.

Qiao, S., Luo, Q., Zhao, Y., Zhang, X.C., and Huang, Y. (2014). Structural basis for lipopolysaccharide insertion in the bacterial outer membrane. Nature *511*, 108–111.

Rohou, A., and Grigorieff, N. (2015). CTFFIND4: Fast and accurate defocus estimation from electron micrographs. J. Struct. Biol. *192*, 216–221.

Sára, M., and Sleytr, U.B. (2000). S-Layer proteins. J. Bacteriol. *182*, 859–868.

Scheres, S.H.W. (2012). RELION: implementation of a Bayesian approach to cryo-EM structure determination. J. Struct. Biol. *180*, 519–530.

Scheres, S.H.W., and Chen, S. (2012). Prevention of overfitting in cryo-EM structure determination. Nat. Methods *9*, 853–854.

Schindelin, J., Arganda-Carreras, I., Frise, E., Kaynig, V., Longair, M., Pietzsch, T., Preibisch, S., Rueden, C., Saalfeld, S., Schmid, B., et al. (2012). Fiji: an open-source platform for biological-image analysis. Nat. Methods *9*, 676–682.

Schrödinger, L.L.C. (2017). The PyMOL Molecular Graphics System, Version 2.0. (Schrödinger LLC).

Schüttelkopf, A.W., and van Aalten, D.M.F. (2004). PRODRG: a tool for high-throughput crystallography of protein-ligand complexes. Acta Crystallogr. D Biol. Crystallogr. *60*, 1355–1363.

Simon, R., Priefer, U., and Pühler, A. (1983). A Broad Host Range Mobilization System for *In Vivo* Genetic Engineering: Transposon Mutagenesis in Gram Negative Bacteria. Nat. Biotechnol. *1*, 784–791.

Sleytr, U.B., Schuster, B., Egelseer, E.-M., and Pum, D. (2014). S-layers: principles and applications. FEMS Microbiol. Rev. *38*, 823–864.

Smit, J., Engelhardt, H., Volker, S., Smith, S.H., and Baumeister, W. (1992). The S-layer of *Caulobacter crescentus*: three-dimensional image reconstruction and structure analysis by electron microscopy. J. Bacteriol. *174*, 6527–6538.

Smit, J., Kaltashov, I.A., Cotter, R.J., Vinogradov, E., Perry, M.B., Haider, H., and Qureshi, N. (2008). Structure of a novel lipid A obtained from the lipopolysaccharide of *Caulobacter crescentus*. Innate Immun. *14*, 25–37.

Steinbacher, S., Baxa, U., Miller, S., Weintraub, A., Seckler, R., and Huber, R. (1996). Crystal structure of phage P22 tailspike protein complexed with *Salmonella* sp. O-antigen receptors. Proc. Natl. Acad. Sci. USA *93*, 10584–10588.

Sumper, M., Berg, E., Mengele, R., and Strobel, I. (1990). Primary structure and glycosylation of the S-layer protein of *Haloferax volcanii*. J. Bacteriol. *172*, 7111–7118.

Turoňová, B., Schur, F.K.M., Wan, W., and Briggs, J.A.G. (2017). Efficient 3D-CTF correction for cryo-electron tomography using NovaCTF improves subtomogram averaging resolution to 3.4Å. J. Struct. Biol. *199*, 187–195.

Walker, S.G., Karunaratne, D.N., Ravenscroft, N., and Smit, J. (1994). Characterization of mutants of Caulobacter crescentus defective in surface attachment of the paracrystalline surface layer. J. Bacteriol. *176*, 6312–6323.

Wan, W., Kolesnikova, L., Clarke, M., Koehler, A., Noda, T., Becker, S., and Briggs, J.A.G. (2017). Structure and assembly of the Ebola virus nucleocapsid. Nature *551*, 394–397.

Zheng, S.Q., Palovcak, E., Armache, J.-P., Verba, K.A., Cheng, Y., and Agard, D.A. (2017). MotionCor2: anisotropic correction of beam-induced motion for improved cryo-electron microscopy. Nat. Methods *14*, 331–332.

Zivanov, J., Nakane, T., Forsberg, B.O., Kimanius, D., Hagen, W.J.H., Lindahl, E., and Scheres, S.H.W. (2018). New tools for automated high-resolution cryo-EM structure determination in RELION-3. eLife *7*, e42166.

STAR★METHODS

KEY RESOURCES TABLE

REAGENT or RESOURCE	SOURCE	IDENTIFIER
Chemicals, Peptides, and Recombinant Proteins		
ethylene glycol bis(2-aminoethyl ether)-*N,N,N′,N′*-tetraacetic acid (EGTA)	SigmaAldrich	Cat#E3889-100G
Fiducial gold (FG) 10 nm, 400 μL	CMC Utrecht	N/A
Critical Commercial Assays		
Pro-Q Emerald 300 Lipopolysaccharide Gel Stain Kit	Thermo Fisher Scientific	Cat#P20495
Deposited Data		
RsaA_{NTD}:PS structure	This study	PDB: 6T72
RsaA_{NTD}:PS cryo-EM map	This study	EMDB: EMD-10389
RsaA S-layer cryo-ET map	This study	EMDB: EMD-10388
Experimental Models: Organisms/Strains		
Escherichia coli S17-1	(Simon et al., 1983)	S 17-1
Escherichia coli Alpha-select™	Bioline	N/A
Caulobacter crescentus strain CB15N (NA1000)	(Evinger and Agabian, 1977)	N/A
Caulobacter crescentus strain YB5754	E. Quardokus, personal communication	YB5754
Caulobacter crescentus strain YB1001	This study	YB1001
Recombinant DNA		
pNPTS138	Brun lab collection	N/A
pNPTS138::*rsaA*TEV250	This study	N/A
pNPTS138Δ*rsaA*	(Hardy et al., 2010)	N/A
Oligonucleotides		
Primers for generation of *rsaA*TEV250 strain (see Table S2 for details)	This study	N/A
Primers for sequencing of mutant *rsaA*TEV250 strain (see Table S2 for details)	This study	N/A
Primers for PCR and sequencing of mutant Δ*rsaA* strain (see Table S2 for details)	This study	N/A
Primers for sequencing mutant plasmid vectors (see Table S2 for details)	This study	N/A
Software and Algorithms		
CCP-EM	(Burnley et al., 2017)	http://www.ccpem.ac.uk/
Coot	(Emsley et al., 2010)	https://www2.mrc-lmb.cam.ac.uk/personal/pemsley/coot/
CTFFIND	(Rohou and Grigorieff, 2015)	https://grigorefflab.janelia.org/ctf
EPU	Thermo Fisher Scientific	https://www.fei.com/software/epu/
Fiji	(Schindelin et al., 2012)	https://fiji.sc/
Gromacs 2019	(Abraham et al., 2015)	http://www.gromacs.org/
IMOD	(Kremer et al., 1996)	http://bio3d.colorado.edu/imod/
MATLAB R2017b	Mathworks	https://uk.mathworks.com/
MotionCor2 (implemented in Relion 3.0)	(Zheng et al., 2017)	N/A
novaCTF	(Turoňová et al., 2017)	https://github.com/turonova/novaCTF
PHENIX	(Adams et al., 2010)	https://www.phenix-online.org/
PRODRG	(Schüttelkopf and van Aalten, 2004)	http://www.gromacs.org/Downloads/Related_Software/PRODRG

(Continued on next page)

Continued

REAGENT or RESOURCE	SOURCE	IDENTIFIER
PyMOL	(Schrödinger, 2017)	https://pymol.org/2/
REFMAC5	(Murshudov et al., 2011)	https://www2.mrc-lmb.cam.ac.uk/groups/murshudov/content/refmac/refmac.html
RELION 3.0	(Zivanov et al., 2018), (Bharat et al., 2015)	https://www2.mrc-lmb.cam.ac.uk/relion
Sequencher 5.4.6	Gene Codes Corporation	https://www.genecodes.com/
SerialEM	(Mastronarde, 2005)	http://bio3d.colorado.edu/SerialEM/
UCSF Chimera	(Pettersen et al., 2004)	https://www.cgl.ucsf.edu/chimera/
Xcalibur 4.2	Thermo Fisher Scientific	N/A
Other		
R2/2 200 mesh Cu/Rh holey carbon grids	Quantifoil	https://www.quantifoil.com/

LEAD CONTACT AND MATERIALS AVAILABILITY

Further information and requests for reagents may be directed to, and will be fulfilled by the Lead Contact, Tanmay A.M. Bharat (tanmay.bharat@path.ox.ac.uk). Strains and reagents generated in this study will be made available on request, but we may require a payment and/or a completed Materials Transfer Agreement if there is potential for commercial application.

EXPERIMENTAL MODEL AND SUBJECT DETAILS

All *C. crescentus* strains listed in this study are listed in the Key Resources table. *C. crescentus* strains were grown in peptone-yeast-extract (PYE) medium (Poindexter, 1964) at 30°C, with antibiotic and carbon supplements at the following concentrations when necessary: kanamycin (5 μg/mL (plate), 5 μg/mL (broth)), nalidixic acid (20 μg/mL (plate)). *Escherichia coli* strains were cultured at 37°C in Luria-Bertani (LB) medium. LB medium was supplemented with kanamycin (25 μg/mL or 25 μg/mL (plate)) when necessary. Bacterial strains and plasmids used in this study are further listed in Table S2.

METHOD DETAILS

DNA manipulations and sequencing

All primers used in this study are listed in Table S2 and were purchased from Eurofins Genomics (Louisville, KY). PCR products were generated using iProoF Hi-Fidelity DNA polymerase (Biorad, Hercules, CA) and purified using Qiaquick spin columns (QIAGEN, Valencia, CA) following procedures recommended by the manufacturer. Chromosomal DNA was isolated using Promega Magic Mini-Prep DNA purification system (Promega, Madison, WI) using the manufacturer's instructions. DNA sequencing was performed by Eurofins Genomics. Sequence data were analyzed using Sequencher 5.4.6 software (Gene Codes Corporation, Ann Arbor, MI).

Construction of *rsaA* mutants

The TEV protease mutants were generated by homologous recombination using upstream and downstream fragments of *rsaA* cloned into a non-replicating plasmid pNPTS138, which carries a kanamycin resistance gene cassette (*nptI*), along with the *sacB* cassette that confers sucrose sensitivity as previously described (Gonin et al., 2000). The TEV protease site (Glu-Asn-Leu-Tyr-Phe-Gln-:-Gly) was engineered at amino acid 250 of RsaA. An upstream ∼2000 bp PCR fragment that contained 1000 bp of upstream DNA and the first 749 bp (250 aa) of *rsaA* was generated using primers, 138rsaA1kbupF and rsaATEV250upR. The downstream ∼2600 bp PCR product that contained the remainder of *rsaA* from 750 to 3080 bp (amino acid residues 251 to 1026) and an additional 500 bp of downstream DNA was created with primers, rsaATEV250dwnF and 138rsaA500dwnR. Gibson Assembly with NEBuilder HiFi Assembly mix (New England Biolabs, Ipswitch, MA) was used to assemble the two PCR products and pNPTS138 digested with EcoRV and treated with calf intestinal alkaline phosphatase (New England Biolabs). The Gibson Assembly reaction was transformed into alpha select silver chemically competent cells (Bioline, Swedesboro, NJ) and selected on LB supplemented with kanamycin. Transformants were screened by PCR using M13F, M13R and TEVprimerF and confirmed by sequencing. Plasmid (pNPTS138::3rsaATEV250) was transformed into S17-1, mated into NA1000 Δ*rsaA* and selected on PYE with nalidixic acid and kanamycin. The additional selection with *sacB* was not utilized here.

The NA1000 *ΔrsaA* mutant was generated by mating pNPTS138Δ*rsaA* into NA1000, plating on PYE with kanamycin and nalidixic acid to select for the primary integrants. The transconjugants were plated on PYE sucrose and the *sacB* gene was used to select for the secondary recombination event and loss of the plasmid. The loss of *rsaA* was screen for by PCR and confirmed by sequencing.

Purification of RsaA_{NTD} protein

Cells from the *C. crescentus rsaA*_{TEV250} strain, containing the genomic TEV-protease cleavage site, were grown in PYE medium (Poindexter, 1964) for 24 hours at 20°C with shaking at 180 rpm. Six liters of the bacterial culture were centrifuged (5000 rcf, 4°C, 30 min). The pelleted cells were re-suspended in 50 mM HEPES/HCl buffer at pH 2.0 on ice for 10 min with vigorous shaking. Next, the suspension was centrifuged (16000 rcf, 4°C, 30 min). The pellet was discarded and the pH of the supernatant was adjusted to 7.0 with 5 M NaOH. The resulting liquid was filtered and loaded onto a 5 mL HiTrap SP HP column (GE Healthcare). All purification steps were performed using an ÄKTA pure 25 M system (GE Healthcare) operating at 4°C. The flow-through from the column was collected and dialyzed against 10 mM Tris/HCl pH 8.0 for 3 hours at 4°C. The dialyzed solution was loaded onto a 5 mL HiTrap Q HP column (GE Healthcare), washed with 20 mM Tris/HCl pH 8.0 and then eluted with the same buffer containing increasing concentrations of NaCl. Fractions containing pure RsaA_{TEV250} were collected and cleaved overnight by addition of His_{6}-TEV protease in a ratio of 1:100 (wt:wt). His_{6}-TEV protease was removed by loading the protein solution to a 5 mL HisTrap FF column (GE Healthcare). The flow-through was collected, concentrated and loaded to a Superdex S200 16/600 (prep grade) column (GE Healthcare) equilibrated with 25 mM HEPES/NaOH pH 7.5, 100 mM, 1 mM CaCl_{2}. RsaA_{NTD} was eluted with the same buffer and fractions containing RsaA_{NTD} were collected and concentrated upto 3.7 mg/mL protein concentration (Amicon 10 kDa MWCO). Aliquots were frozen in liquid nitrogen and stored at −80°C.

Purification of full length RsaA

Wild-type RsaA protein was purified as described previously (Bharat et al., 2017) with modifications as follows: *C. crescentus* CB15N (NA1000) cells were grown in PYE medium for 24 hours at 25°C with shaking. The resulting culture (4 L) was centrifuged (5000 rcf, 4°C, 30 min) and the pelleted cells were re-suspended in 50 mM HEPES/HCl buffer at pH 2.0 on ice for 10 min with vigorous shaking. Next, the suspension was centrifuged (16000 rcf, 4°C, 30 min) and the cell pellet was discarded. The pH of the supernatant was adjusted to 7.0 with 5 M NaOH, filtered and loaded onto a 5 mL HiTrap SP HP column (GE Healthcare). The flow-through from the column was collected and dialyzed against 10 mM Tris/HCl pH 8.0 overnight at 4°C. The dialyzed protein solution was loaded onto a 5 mL HiTrap Q HP column (GE Healthcare), washed with 20 mM Tris/HCl pH 8.0 and then eluted with the same buffer containing increasing concentrations of NaCl. Fractions containing pure RsaA were collected and dialyzed against 20 mM Tricine/NaOH pH 8.0 and then concentrated to ∼25 mg/mL. Aliquots were flash frozen in liquid nitrogen and stored at −80°C.

Purification of crude LPS from *C. crescentus*

Crude LPS was purified as described previously (Jones et al., 2015), with a few modifications as follows. Crude LPS was purified from a *C. crescentus* Δ*rsaA* strain, cells were grown in PYE medium for 24 hours at 30°C with shaking at 180 rpm. Two liters of the bacterial culture were centrifuged (5000 rcf, 4°C, 30 min). The pelleted cells were washed once with 1x phosphate buffered saline (PBS) and recentrifuged (16000 rcf, 4°C, 30 min). Pelleted cells were resuspended in 60 mL of PBS supplemented with 35 mM EDTA to extract LPS from the cell surface under gentle agitation. Cells were removed by two consecutive centrifugation steps (16000 rcf, 4°C, 30 min) and resulting supernatant was treated with 50 μg/mL DNaseI and 1 U/mL benzonase (Sigma Aldrich) and dialysed against 5 mM MgCl_{2} for 4 hours at 25°C. Proteinase K was added to the dialysed solution to a final concentration of 0.01 mg/mL and incubated at 50°C overnight. The proteinase K treated sample was clarified by two centrifugation steps (50000 rcf, 4°C, 1 hour and 200000 rcf, 4°C, 3 hours). Aliquots of the resulting supernatant and pellet fractions were analyzed by sodium dodecyl sulphate-polyacrylamide gel electrophoresis (SDS-PAGE) and stained with Pro-Q Emerald 300 Lipopolysaccharide Gel Stain Kit (ThermoFisher). While a minor fraction of the isolated LPS was lost in the pellet, the majority was found in the supernatant which was concentrated 120 times (Amicon 3.5 kDa MWCO) and loaded onto a Superose 6 10/300 GL column (GE Healthcare) equilibrated with 200 mM NaCl. Crude LPS was eluted with the same buffer and monitored at a wavelength of 215 nm. Fractions containing high absorbance were collected and analyzed by SDS-PAGE and Pro-Q Emerald 300 staining and Coomassie brilliant blue G-250. Aliquots containing crude LPS were flash frozen in liquid nitrogen and stored at −80°C.

Reconstitution of the RsaA_{NTD}:PS complex

PS was partially released from purified, crude LPS by hydrolysis with acetic acid (1% (v/v), 95°C, 2 hours). The sample was clarified by centrifugation (16000 rcf, 4°C, 30 min) and adjusted to pH 7.0 by addition of 1 M HEPES/NaOH pH 7.0. An excess of purified RsaA_{NTD} was mixed with hydrolysed PS and the mixture was dialyzed against 25 mM HEPES/NaOH pH 7.5, 100 mM NaCl, 1mM MgCl_{2}, 1mM CaCl_{2} overnight at 4°C. The sample was loaded to a Superose 6 10/300 GL column (GE Healthcare) equilibrated with the same buffer. Peak fractions containing oligomeric RsaA_{NTD} were collected, concentrated (Amicon 30 kDa MWCO) and flash frozen in liquid nitrogen and stored at −80°C.

Preparation of samples for cellular cryo-ET

For cellular cryo-ET (Figure 4), CB15N *C. crescentus* cells or cells with genomic deletion of *rsaA* (Δ*rsaA* strain), were grown in PYE medium to late log phase at 30°C with vigorous shaking and directly used for grid preparations. For probing binding of RsaA to cellular LPS, Δ*rsaA* cells were mixed with purified RsaA$_{NTD}$ (∼1 mg/mL final concentration) or with RsaA (full-length) protein (∼2.5 mg/mL final concentration). Cells were incubated with vigorous shaking for 15 min at room temperature before vitrification. Ca^{2+} dependence of RsaA$_{NTD}$ binding to the cell surfaces was tested by centrifuging 5 mL of late log phase Δ*rsaA* cells (16000 rcf, 25°C, 10 min) and resuspending the pellet in the 5 mL of liquid containing 10 mM HEPES pH 7.5, 5 mM ethylene glycol bis(2-aminoethyl ether)-*N,N,N′,N′*-tetraacetic acid (EGTA). This process was repeated three times, and the sample was mixed with purified RsaA$_{NTD}$ (∼1 mg/mL final concentration) and incubated at room temperature with vigorous shaking for 15 min before vitrification.

Cryo-EM and cryo-ET sample preparation

For cryo-EM grid preparation 2.5 μL of purified RsaA$_{NTD}$ or RsaA$_{NTD}$:PS complex (2.5 mg/mL) was applied to a freshly glow discharged Quantifoil R2/2 Cu/Rh 200 mesh grid, adsorbed for 10 s, blotted for 3 s and plunge-frozen into liquid ethane in a Vitrobot Mark IV (ThermoFisher), while the blotting chamber was maintained at 100% humidity at 10°C. For cryo-ET sample preparation, purified or cellular samples were mixed with 10 nm protein-A gold (CMC Utrecht) before application to the cryo-EM grid.

Cryo-EM and cryo-ET data collection

Single-particle cryo-EM data was collected on a Titan Krios G3 microscope (ThermoFisher) operating at 300 kV fitted with a Quantum energy filter (slit width 20 eV) and a K2 direct electron detector (Gatan) with a sampling pixel size of 1.08 Å running in counting mode. In total 2422 movies were collected with a dose rate of 6.3 e⁻/pixel/s on the camera level. The sample was subjected to 8 s of exposure where a total dose of 43 e⁻/Å^2 was applied, and 20 frames were recorded per movie. Data collection for initial model generation using sub-tomogram was performed on the same Titan Krios microscope using the Quantum energy filter (slit width 30 eV) and the K2 direct electron detector running in counting mode with a dose rate of 5.5 e⁻/pixel/s (Gatan). Tilt series (6 in total) with a defocus range of −3 to −6 μm were collected between ± 60° in two directions from 0° at 2° tilt increment. A total dose of 100 e⁻/Å^2 was applied over the entire series, and image data was sampled at a calibrated pixel size of 2.238 Å. For cellular samples, tilt series (wt: 10 tilt series; Δ*rsaA*: 13 tilt series; Δ*rsaA* + RsaA$_{NTD}$: 7 tilt series; Δ*rsaA* + RsaA: 2 tilt series) were collected at a dose rate of 11.3 e⁻/pixel/s, with a total dose over the series of 81 e⁻/Å^2. Data was sampled at a calibrated pixel size of 5.571 Å using the K2 direct electron detector running in counting mode (slit width 20 eV). For high-resolution *in situ* structure determination of the S-layer, a pipeline for high-throughput data collection was adopted (Wan et al., 2017). Briefly, a Titan Krios microscope was used to collect tilt series data with a dose symmetric tilting scheme (Hagen et al., 2017). Tilt series were collected at a pixel size of 1.3 Å, with a total dose of 140 e⁻/Å^2 was applied over entire series collected between ± 60° with 3° tilt increments (Bharat et al., 2017).

Cryo-EM single-particle image processing

Initial model generation from cryo-ET data was performed using the Relion sub-tomogram averaging pipeline (Bharat et al., 2015; Bharat and Scheres, 2016). An unambiguous 3D reference was generated and used in the single-particle EM pipeline as follows. Movies were motion corrected and dose weighted with MotionCor2 (Zheng et al., 2017) implemented in Relion 3.0 (Zivanov et al., 2018). Contrast transfer functions (CTFs) of the resulting motion corrected micrographs were estimated using CTFFIND4 (Rohou and Grigorieff, 2015). Particles were extracted with a 300 pixel × 300 pixel box and classified using reference-free 2D-classification inside Relion 3.0. Particles from classes showing high-resolution features were subjected to 3D classification using the unbiased sub-tomogram averaging reference structure described above. Particles from two main 3D classes containing 21 or 20 RsaA$_{NTD}$ subunits were combined for a focused 3D auto refinement on the central 14 subunits using the output from the 3D classification as a starting model. The final map was obtained from 115,776 particles and post-processed using a soft mask focused on the inner fourteen subunits yielding a sharpened map with a *B*-factor of −85.8 Å^2 and a resolution of 3.68 Å according to the gold standard Fourier shell correlation criterion of 0.143 (Scheres and Chen, 2012).

Sub-tomogram averaging

Tilt series alignment using gold fiducials and tomogram generation was carried out using IMOD (Kremer et al., 1996). Sub-tomogram averaging processing was performed using custom scripts written in MATLAB, described in detail elsewhere (Bharat et al., 2011; Wan et al., 2017). Cellular sub-tomogram averages (see Figures 4 and S5) were lowpass filtered to the same resolution of 40 Å for comparison. For high-resolution cryo-ET structure determination, we adopted previously published methods (Bharat et al., 2017) with the major difference being the use of a recently developed in 3D-CTF correction method for tomographic data (Turoňová et al., 2017). In addition, we used focused alignment on the RsaA$_{NTD}$ part of the S-layer to improve this region of the map to observe LPS binding. The final map was obtained from 51,866 hexameric units of the S-layer from 110 tomograms (Bharat et al., 2017). Post-processing using a softened mask focused on the inner domain and pore region of RsaA yielded a sharpened map with a *B*-factor of −224.953 Å^2 applied and a resolution of 4.82 Å (Figure S6) according to the 0.143 criterion. The final map has not been explicitly symmetrized and local resolution differences were estimated in Relion 3.0. Figures were prepared using Fiji (Schindelin et al., 2012) and MATLAB.

Model building and refinement

The carbon backbone of the RsaA$_{NTD}$ protein was manually traced through a single subunit of the cryo-EM density using Coot (Emsley et al., 2010). Initially, side chains were assigned in regions with density corresponding to characteristic aromatic residues allowing us to deduce the register of the amino acid sequence in the map. Side chains for residues 2-243 of RsaA were thus assigned unambiguously and the structure was refined and manually rebuilt using Refmac5 (Murshudov et al., 2011) inside the CCP-EM (Burnley et al., 2017) software suite and Coot. Additional subunits around the spiral of the RsaA$_{NTD}$:PS complex were generated by rigid body fitting the refined monomeric unit into the cryo-EM density. Areas of strong and continuous density connecting protein subunits along the long axis of the spiral could not be explained by any amino acid residues in RsaA$_{NTD}$ and were therefore assigned to the O-antigen of the *C. crescentus* LPS, to which RsaA$_{NTD}$ is known to bind (Bharat et al., 2017; Ford et al., 2007). The chemistry of the heptameric repeating unit of the O-antigen has been described previously (Jones et al., 2015), and was used to build the main chain of the PS. Orientation of the PS was assigned by iterative rebuilding and refinement using restraints for N-Acetyl-perosamine (PerNac) which were generated with PRODRG (Schüttelkopf and van Aalten, 2004) and existing restraints for mannose. Comprehensive model validation of the final structure and map was performed in PHENIX (Adams et al., 2010) (see Table S1). The final refined cryo-EM structure of RsaA$_{NTD}$ and the X-ray structure of RsaA$_{CTD}$ (PDB ID 5N8P) were rigid body docked into the 4.8 Å cryo-ET map and were not refined further. Figures containing protein structures or cryo-EM/ET data were prepared using USCF Chimera (Pettersen et al., 2004).

Native mass spectrometry

Samples were loaded into a gold coated needle prepared in-house and introduced into a Q-Exactive UHMR mass spectrometer (ThermoFisher), as described previously (Gault et al., 2016). The following parameters were used: capillary voltage was set to 1.2-1.4 kV, resolution was set to 17500 at m/z 200, injection flatopole was set to 5 V, inter flatopole lens was at 4 V, and bent flatopole at 2 V. Backing pressure was maintained at $\sim 3 \times 10^{-9}$ mbar. Stripped oligomers were obtained by MS/MS analysis at a voltage applied to the HCD cell of 220 V. Zeba^{TM} micro spin desalting columns were used to remove the Ca^{2+} ions. Data was analyzed using Xcalibur 4.2.

Molecular dynamics simulations

Atomistic simulations were run in triplicate for 100 ns using the CHARMM36m forcefield (Huang et al., 2017). Simulations were performed at 310 K using the velocity-rescaling temperature coupling algorithm (Bussi et al., 2007), with a time constant of 0.1 ps and Parrinello-Rahman isotropic pressure coupling of 1 bar with a time constant of 2 ps (Parrinello and Rahman, 1981). Electrostatics were handled using the Particle-Mesh-Ewald method (Darden et al., 1993), and a force-switch modifier was applied to the Van der Waals forces. Dispersion corrections were turned off. The parameters for the O-antigen were generated using the CHARMM-GUI (Kim et al., 2017; Lee et al., 2016). All simulations were run using Gromacs 2019 (Abraham et al., 2015). Molecular simulation images and Supplemental Movies of simulations were made in PyMOL (Schrödinger, 2017). Graphs were plotted using Python and Matplotlib.

QUANTIFICATION AND STATISTICAL ANALYSIS

See METHOD DETAILS for further information on the statistical analyses including replicates for MD simulations and resolution estimates for cryo-EM maps.

DATA AND CODE AVAILABILITY

Data resources

The cryo-EM map of RsaA$_{NTD}$:PS complex together with the build atomic model have been deposited in the Electron Microscopy Data Bank (EMDB) with the accession code EMD-10389 and the Protein Data Bank (PDB) with accession code 6T72 respectively. The cryo-ET map of the native S-layer has been deposited with the EMDB accession code EMD-10388.

Software

All software used in this study has been extensively described in previous publications from our and other laboratories. See the METHOD DETAILS section for citations to the original publications.
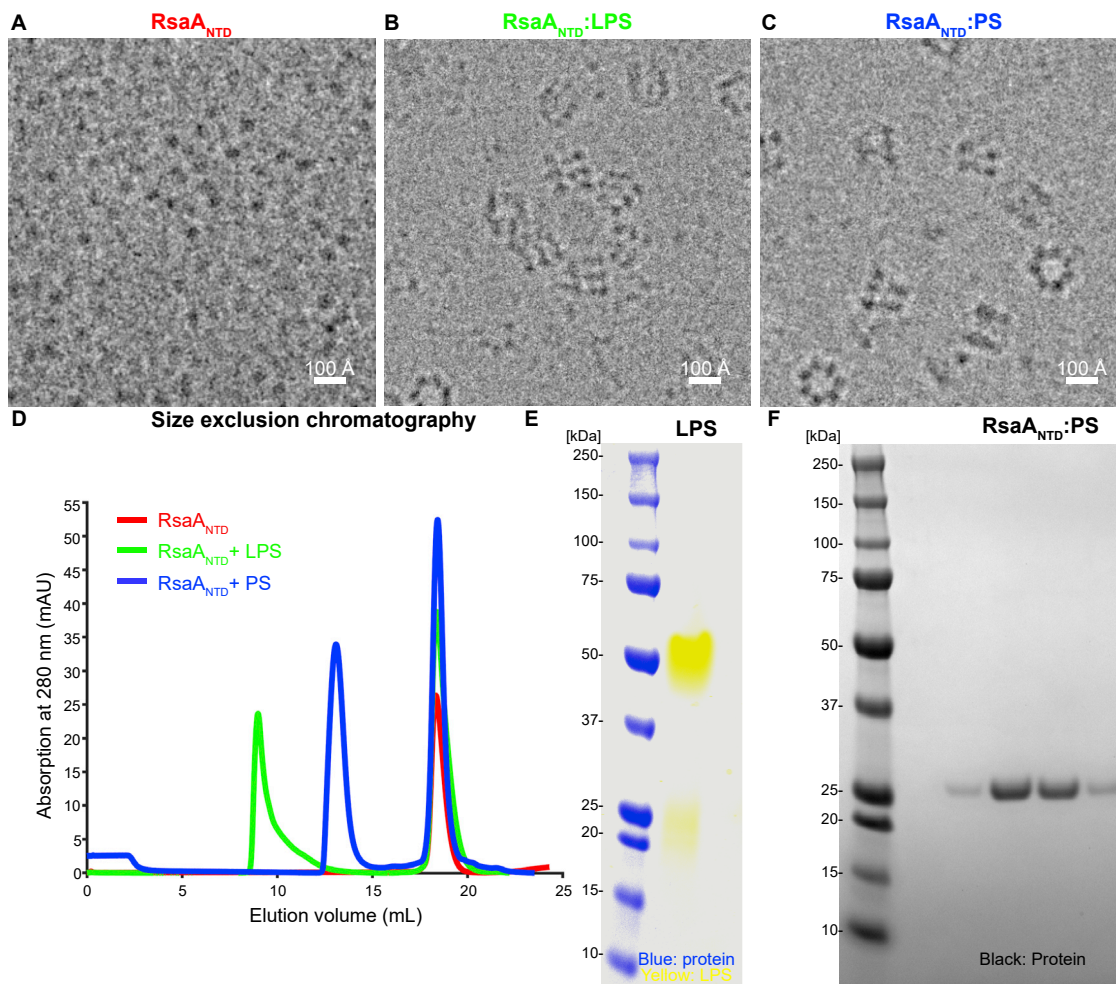
Figure S1. Biochemical Reconstitution of the RsaA_{NTD}:PS Complex, Related to Figure 1

(A) Cryo-EM image of purified monomeric RsaA_{NTD}.

(B) Image of reconstituted oligomeric RsaA_{NTD}:crude LPS aggregate complex.

(C) Cryo-EM image of purified RsaA_{NTD}:PS complex.

(D) Gel-filtration profiles of monomeric RsaA_{NTD} (red), RsaA_{NTD} + crude LPS (green) and RsaA_{NTD} + PS (blue) corresponding to images in (A–C).

(E) SDS-PAGE of purified crude LPS stained with Pro-Q Emerald 300 (yellow) overlaid with the same gel stained with Coomassie brilliant blue G-250 (blue).

(F) SDS-PAGE analysis of purified and mass-spectrometry verified RsaA_{NTD}:PS sample stained with Coomassie brilliant blue G-250 (black).
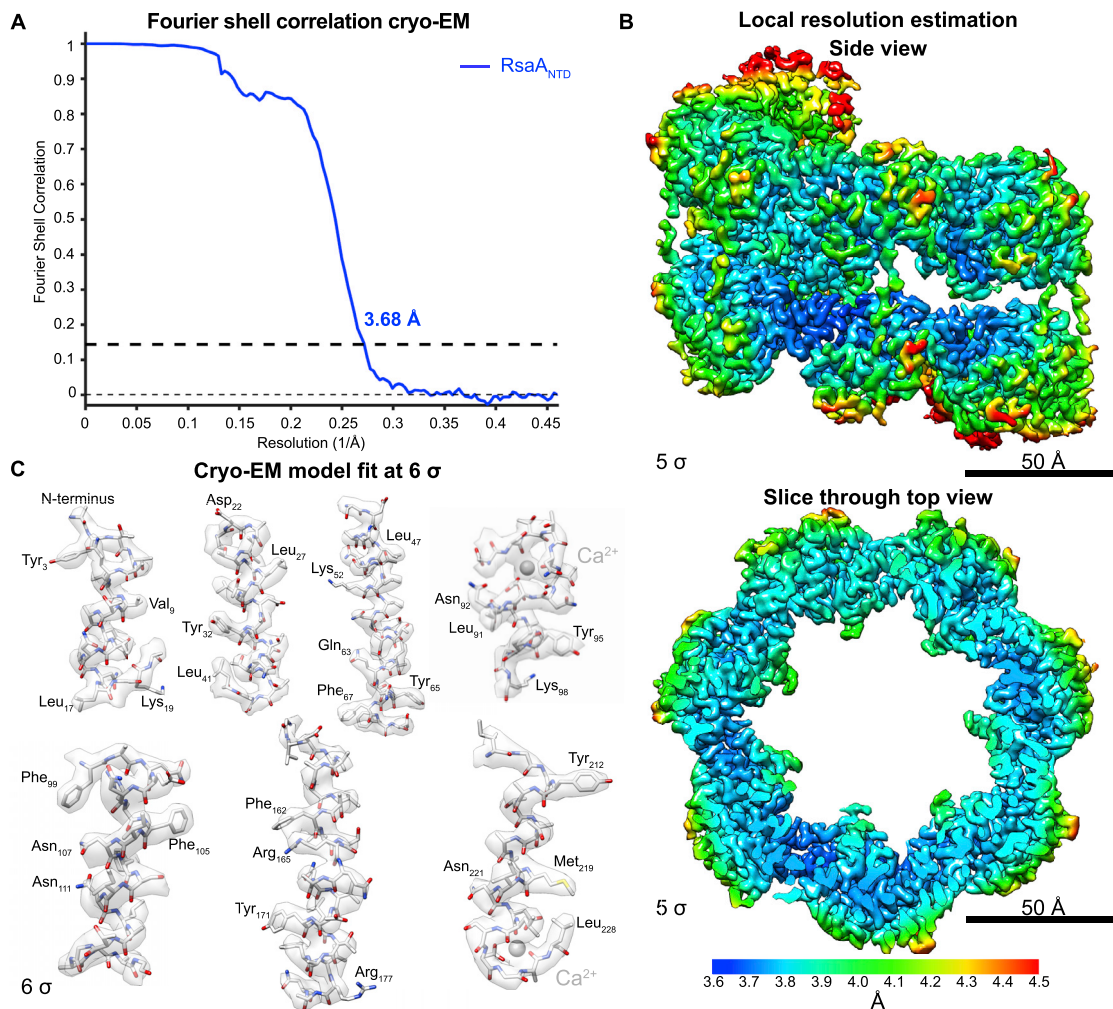
Figure S2. Single-Particle Cryo-EM Reconstruction of the RsaA$_{NTD}$:PS Complex, Related to Figure 1

(A) Fourier shell correlation (FSC) curve of two random half sets of the final reconstructed RsaA$_{NTD}$:PS map shows better than 3.7 Å resolution according to the gold standard criterion of 0.143.

(B) Local resolution differences plotted on the cryo-EM density of the RsaA$_{NTD}$:PS complex.

(C) Examples of the *de novo* built atomic model fitted into the density contoured at 6 σ away from the mean.
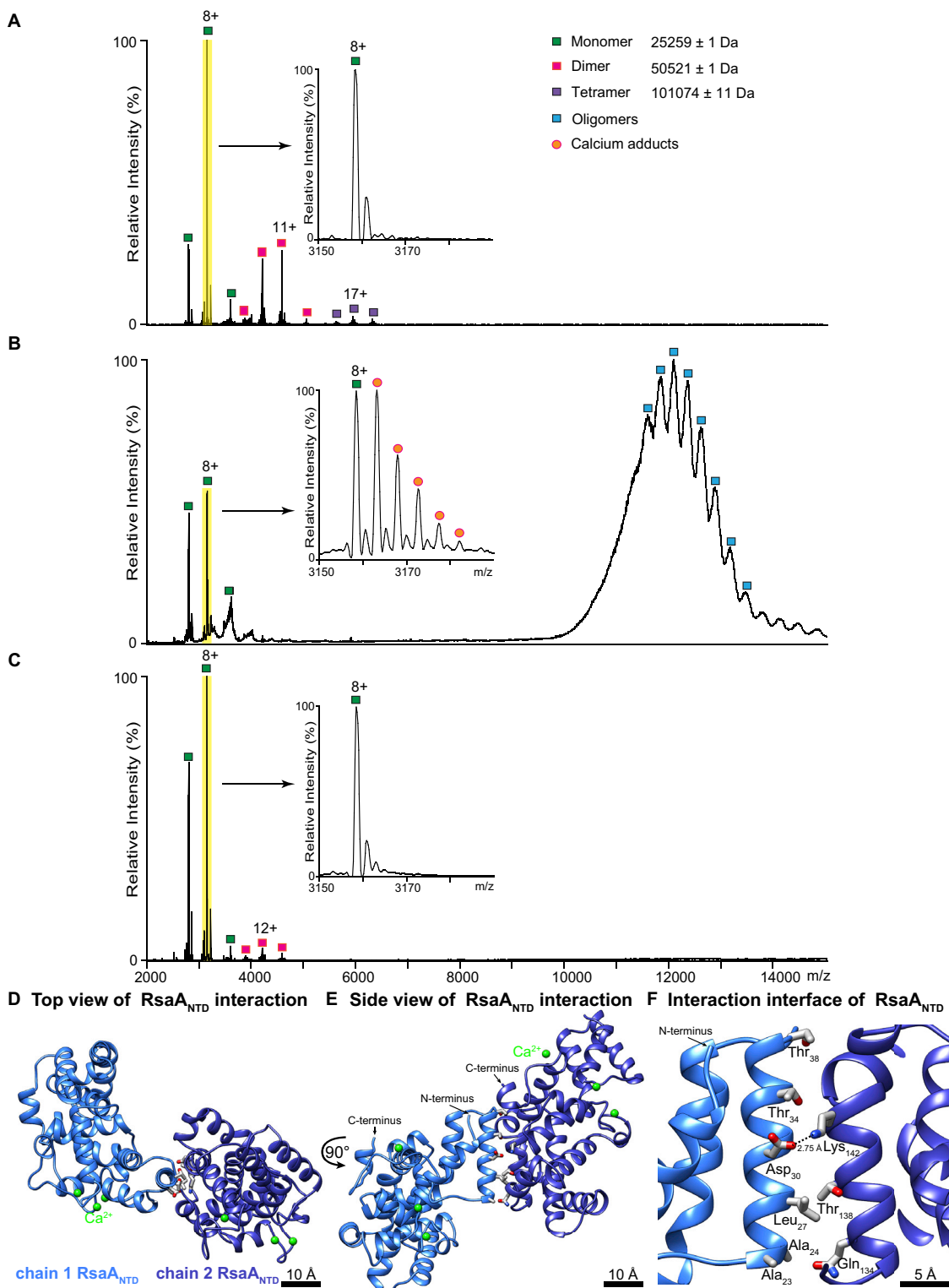
Figure S3. Investigation of the Effect of Ca²⁺ on RsaA$_{NTD}$ Oligomerisation, Related to Figure 2

(A) Mass spectrum of the RsaA$_{NTD}$:PS sample after Ca²⁺ removal shows presence of RsaA$_{NTD}$ monomers, dimers, and tetramers only. Panel same as Figure 2B, shown here for clarity.

(B) Mass spectrum of the above sample following incubation with 1 mM calcium acetate indicates that Ca²⁺ ions stimulate the formation of oligomers (RsaA$_{NTD}$:PS complex).

(legend continued on next page)

(C) After a second Ca^{2+} removal, the complex falls apart into $RsaA_{NTD}$ monomers and dimers.

(D) Top view of the $RsaA_{NTD}$:$RsaA_{NTD}$ interaction interface in the cryo-EM structure shown as ribbon diagram. A single α-helix of one $RsaA_{NTD}$ subunit forms the interaction interface with the next $RsaA_{NTD}$ subunit. This interaction is duplicated around the spiral or in the native S-layer hexamer, likely giving large net stabilization. (E) A 90° rotated side view of (D) along the axis of the $RsaA_{NTD}$:PS spiral is shown.

(F) Close-up view of (E) highlighting key residues at the $RsaA_{NTD}$:$RsaA_{NTD}$ interaction interface. The interface is stabilized by an ionic interaction between Asp_{30} of one $RsaA_{NTD}$ monomer with Lys_{142} of another $RsaA_{NTD}$ molecule.
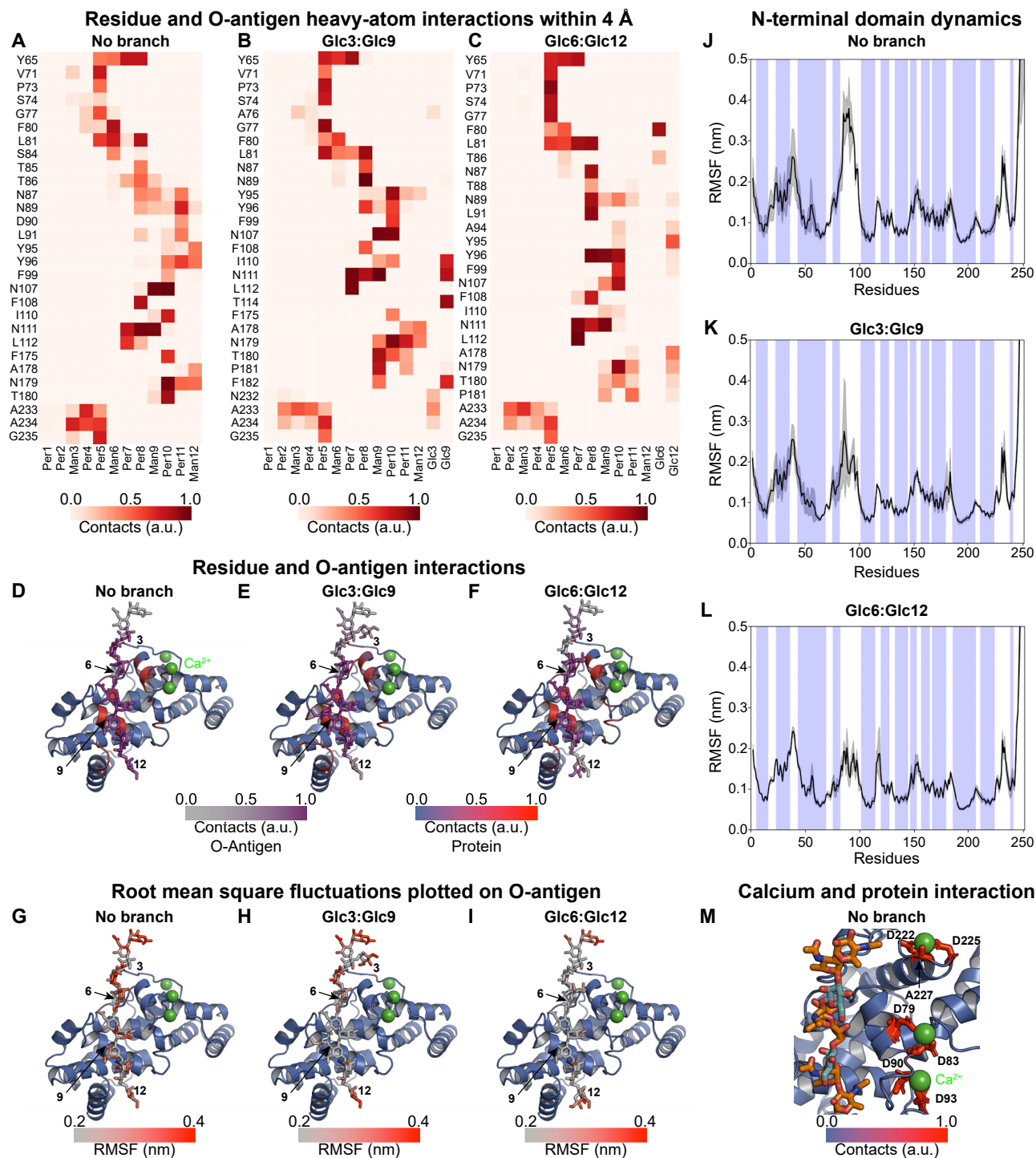
Figure S4. MD Simulations of RsaA_NTD Binding to O-antigen, Related to Figure 3

(A) Plot of amino acid residue and O-antigen (heavy-atom) interactions within 4 Å over the course of three 100 ns simulations. The protein-sugar interactions are normalized to 1 (brown), where 0 (white) relates to no contacts.

(B) Interaction plot of protein residues and O-antigen with branching Glc moieties at the positions 3 and 9.

(C) Protein and O-antigen interactions with branching Glc moieties at the positions 6 and 12.

(D–F) Protein and O-antigen interactions from (A–C) are plotted on the ribbon diagram of the protein on a blue to red scale and on the O-antigen on a gray to purple scale.

(legend continued on next page)

(G–I) Root mean square fluctuations (RMSF) of the O-antigen are displayed on the O-antigen stick diagram on a gray to red color scale (corresponding representation to data in Figures 3D–3F).

(J–L) Plot of RMSF of the RsaA$_{NTD}$ residues (see Figures 3A–3C), showing stabilization of the Ca^{2+} binding loop (residues 77–100) by the branching Glc moieties over the course of three 100 ns simulations (α-helical residues in blue background).

(M) Interaction of protein residues with Ca^{2+} ions during MD simulations shown on a blue to red scale. All Ca^{2+} ions are stabilized by two aspartic acid residues and backbone carbonyl oxygens in the simulations, as well as in our cryo-EM structure.
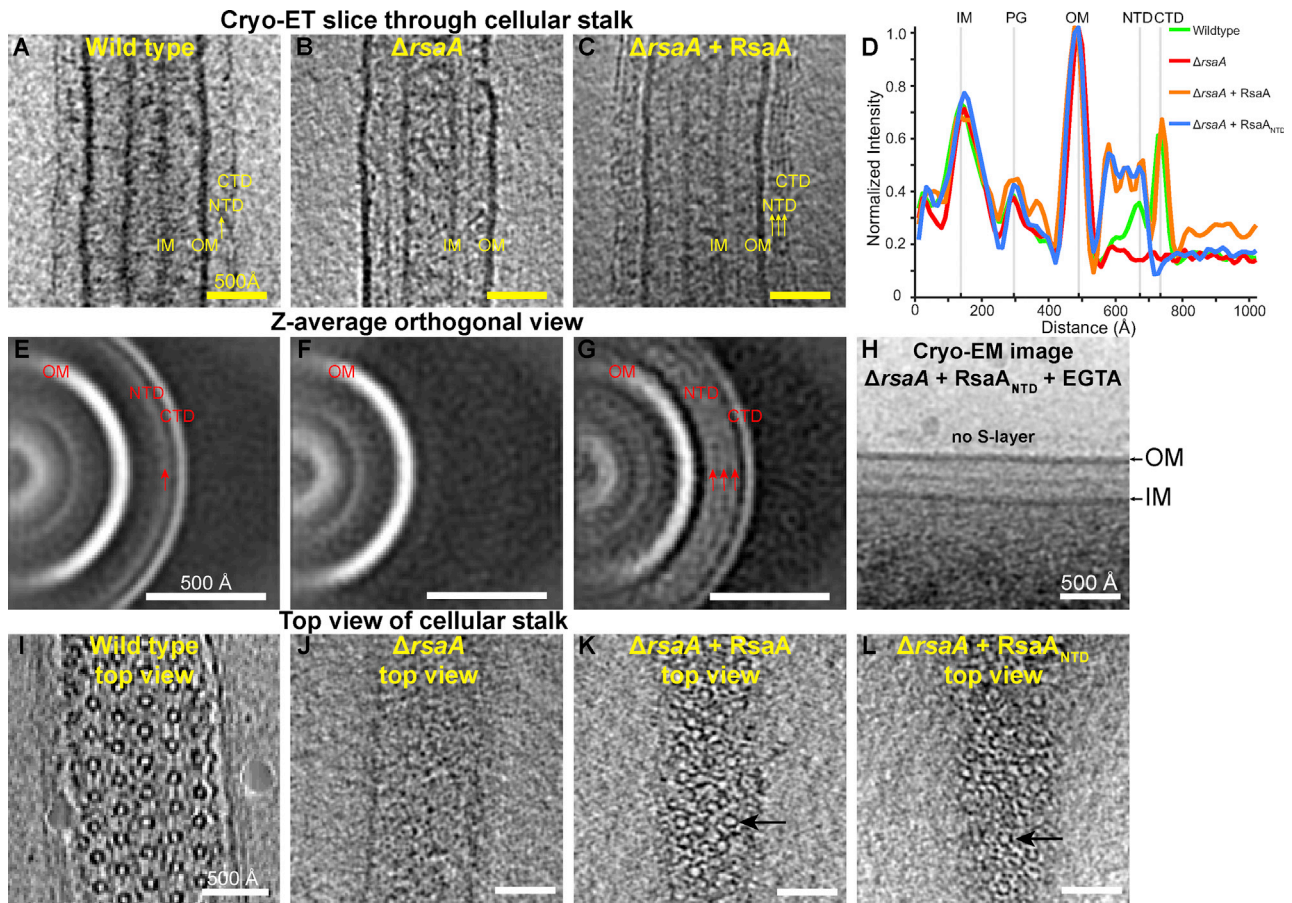
Figure S5. Probing RsaA Binding to Cellular LPS, Related to Figure 4

(A) Cryo-ET slice through a cellular stalk of *C. crescentus*.

(B) Slice through a cell stalk lacking RsaA (Δ*rsaA*).

(C) Slice through a Δ*rsaA* cell stalk with exogenous full-length RsaA added. Decoration of the LPS in three layers is observed (as in Figures 4E and 4F); however, an additional fourth density layer is observed at the same distance from the OM as the native S-layer RsaA$_{CTD}$. This suggests that RsaA molecules bound to the tip of O-antigen form at least a partial outer S-layer lattice by oligomerization of RsaA$_{CTD}$.

(D) Normalized density profiles through subtomogram averages of (A–C) aligned to the OM showing that exogenous added full-length RsaA binds to the entire length of the O-antigen, while forming a partial outer S-layer lattice.

(E–G) Corresponding sub-tomogram averages of (A–C) (Figures S5A and S5B; E–G are the same as Figures 4A–4D, shown here for clarity).

(H) Cryo-EM image of a Δ*rsaA* cell with exogenous RsaA$_{NTD}$ added together with EGTA. Chelation of Ca^{2+} by EGTA prevents S-layer assembly at the cell surface.

(I) Cryo-ET slice through the top of a cell stalk of *C. crescentus* showing a normal, hexagonal S-layer.

(J) Slice though the top of a cell stalk lacking RsaA (Δ*rsaA*).

(K) Slice through the top of a Δ*rsaA* cell stalk with exogenous full-length RsaA added showing irregularly arranged spiral-like structures (black arrow).

(L) Slice through the top of a Δ*rsaA* cell stalk with exogenous RsaA$_{NTD}$ added showing irregularly arranged spiral-like structures (arrow) with characteristics similar to the RsaA$_{NTD}$:PS complex.

A Fourier shell correlation cryo-ET

B Local resolution estimation
Top view

Side view

C Pore region

D Side view of cryo-ET fit

E Top view of monomer
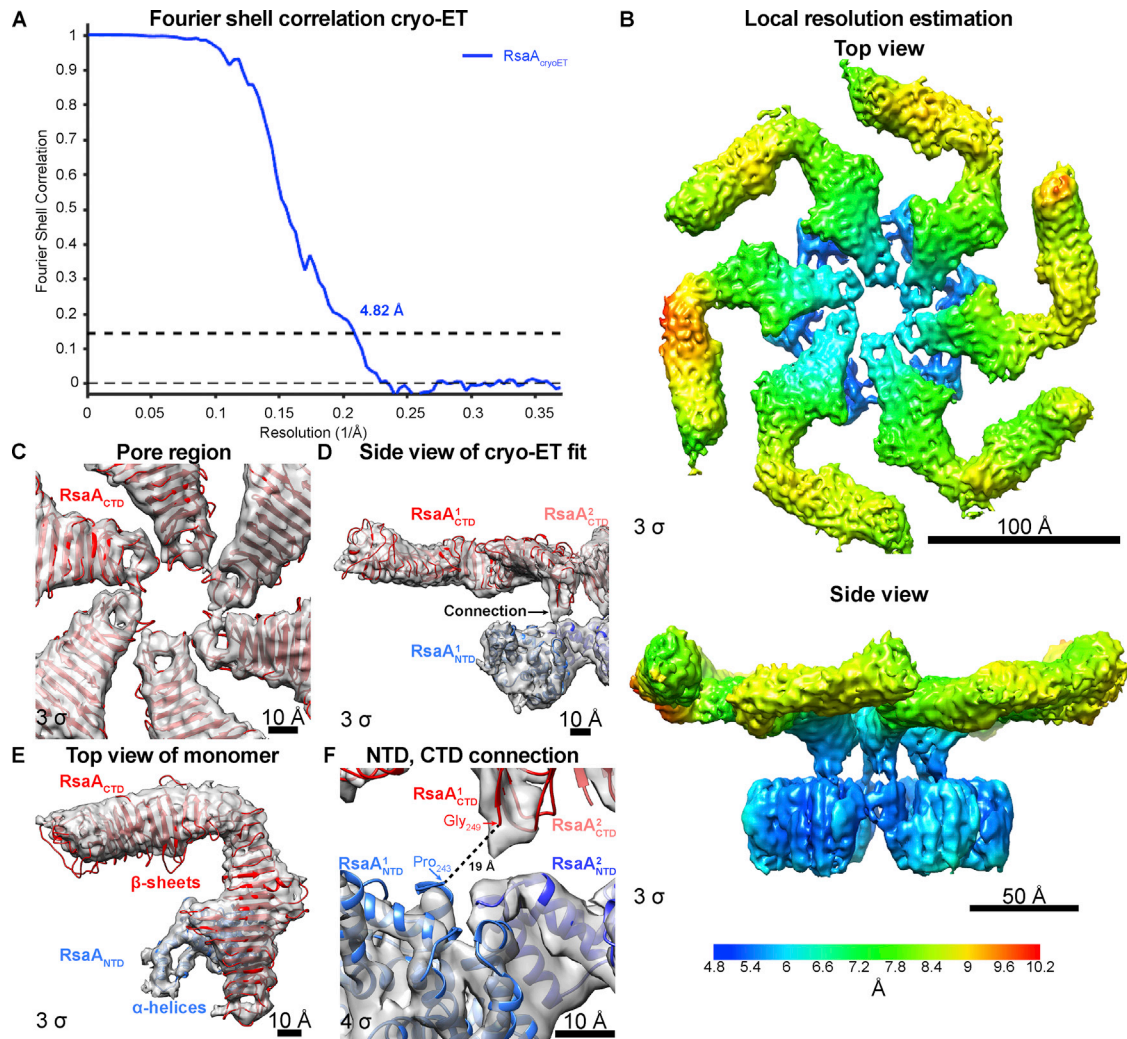
F NTD, CTD connection

Figure S6. Structure of the Native *C. crescentus* S-Layer Determined by Subtomogram Averaging, Related to Figure 5

(A) Fourier shell correlation (FSC) curve of two half sets of the final reconstructed native RsaA S-layer at a 4.82 Å resolution according to the 0.143 criterion.

(B) Local resolution differences plotted on the cryo-ET density showing resolution anisotropy between RsaA$_{NTD}$ and RsaA$_{CTD}$.

(C) Atomic models docked into the cryo-ET density (gray) (contour levels on lower left side of panel). The RsaA$_{CTD}$ X-ray structure (PDB: ID 5N8P) fits the central pore region exceptionally well.

(D) A side view cross-section of the isosurface (gray) is shown with the docked RsaA$_{CTD}$ X-ray structure (red) and the RsaA$_{NTD}$ cryo-EM structure (blue). RsaA$_{CTD}$ is connected to RsaA$_{NTD}$ by a small linker region.

(E) A single monomer of the native RsaA S-layer is shown as top view as in Figure 5B.

(F) Close up view of the connecting region as shown in (D) highlights the exceptional model fit of both domains. The C terminus of the solved cryo-EM structure (Pro$_{243}$) is ~19 Å away from the N terminus (Gly$_{249}$) of the X-ray structure (red). The linker region consisting of five residues is poorly resolved indicating flexibility.

A Cryo-ET slice of cell body

B Cryo-ET slice of cell stalk

C Top view cell body

D Top view cell stalk

E Z-average cell body

F Z-average cell stalk

G RsaA dimer in planar lattice
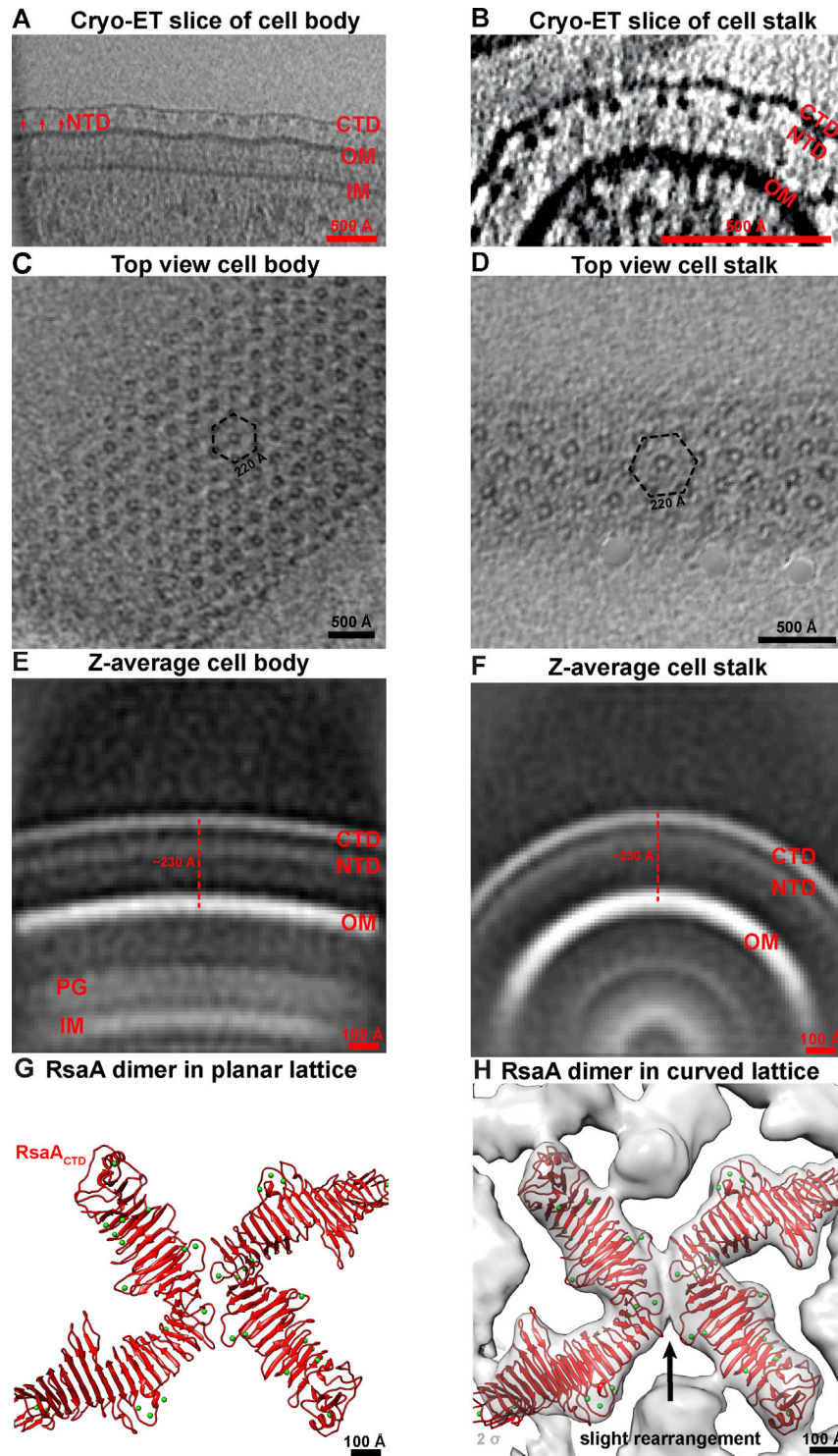
H RsaA dimer in curved lattice

Figure S7. Overall S-Layer Arrangement on the Flat Cell Body and Highly Curved Cell Stalk Is the Same, Related to Figure 6

(A) A cryo-ET slice through the side of a *C. crescentus* cell body (protein density black in all raw cryo-ET slices). The OM is clearly decorated with a S-layer made up of RsaA$_{NTD}$ and RsaA$_{CTD}$ layers (marked).

(B) Cryo-ET slice through the tip of a *C. crescentus* cell stalk. The highly curved OM is covered by a S-layer, consisting of the same RsaA$_{NTD}$ and RsaA$_{CTD}$ layers, with same ultrastructural morphology as the S-layer on the cell body.

(C) Cryo-ET slice through the top surface of a *C. crescentus* cell body. The near hexagonal planar arrangement of the S-layer with a hexamer:hexamer distance of 220 Å is seen, as shown previously (Bharat et al., 2017) and confirmed in this study.

(legend continued on next page)

(D) Cryo-ET slice through the top of a *C. crescentus* cell stalk. Although the S-layer lattice is highly curved around the stalk, the pseudo-hexagonal arrangement of the S-layer with a hexamer:hexamer distance of 220 Å is observed, same as the cell body.

(E) Despite considerably increased specimen thickness, we performed subtomogram averaging of the outer surface of the *C. crescentus* cell body, which shows clear densities for the OM, $RsaA_{NTD}$, and $RsaA_{CTD}$ (protein density white in all averages). The distance between the OM and the $RsaA_{CTD}$ layer is ~230 Å.

(F) Subtomogram averaging of the cell stalk (as shown in Figure 4B) shows a highly curved OM, surrounded by a S-layer. The distance between the OM and the $RsaA_{CTD}$ layer is ~230 Å, same as the cell body, indicating the length of the LPS underneath the S-layer is the same between the stalk and the cell body.

(G) The dimeric $RsaA_{CTD}$ interface observed in the outer S-layer lattice in flat planar sheets, solved by X-ray crystallography (PDB: 5N8P).

(H) Two copies of $RsaA_{CTD}$ were fitted separately into a subtomogram averaging map produced from curved cell stalks with a large box size to visualize the hexamer:hexamer interfaces. The fit shows a mismatch between the X-ray structure and the subtomogram averaging map, suggesting rearrangement of residues at the dimeric interface concurrent with lattice curvature.